Implementation and verification of a user-defined element (UEL) for coupled thermal-hydraulic-mechanical-chemical (THMC) processes in saturated geological media

Xiang Zhou[1], Yida Zhang[2*]

ABSTRACT

Efficient and accurate modeling of the coupled thermal-hydraulic-mechanical-chemical (THMC) processes in various rock formations is indispensable for designing energy geo-structures such as underground repositories for high-level nuclear wastes. This work focuses on developing and verifying an implicit finite element solver for generic coupled THMC problems in geological settings. Starting from the mass, momentum, and energy balance laws, a specialized set of governing equations and a thermoporoelastic constitutive model is derived. This system is then solved by an implicit finite element (FE) scheme. Specifically, the residuals and the Jacobians are scripted in a user-defined element (UEL) subroutine which is then combined with the general-purpose FE software Abaqus Standard to solve initial-boundary value problems. Considering the complexity of the system, the UEL development follows a stepwise manner by first solving the coupled hydraulic-mechanical (HM) and thermal-hydraulic-mechanical (THM) equations before moving on to the full THMC problem. Each implementation step consists of at least one verification test by comparing computed results with closed-form analytical solutions to ensure that the various coupling effects are correctly realized. To demonstrate the robustness of the algorithm and to validate the UEL, a three-dimensional case study is performed with reference to the in-situ heating test of ATLAS at Belgium in 1980s. A hypothetical radionuclide leakage event is then simulated by activating the chemical-concentration degree of freedom and prescribing a constant high concentration at the heater's surface. The model predicts a limited contaminated regime after six years considering both diffusion and advection effects on species transport.

Key words: THMC coupling, finite element, nuclear waste storage, thermal pressurization

[1] Engineering Analyst, Cronus Technology Inc., Houston, TX, USA
[2]Assistant Professor, Department of Civil, Environmental and Architectural Engineering, University of Colorado Boulder, Boulder, CO, USA.
[*] Corresponding author. Email: yida.zhang@colorado.edu

This is the author manuscript accepted for publication and has undergone full peer review but has not been through the copyediting, typesetting, pagination and proofreading process, which may lead to differences between this version and the Version of Record. Please cite this article as doi: 10.1002/nag.3556.

1. Introduction

Safe and permanent storage of spent nuclear fuel and other high-level radioactive wastes (HLWs) has been a pressing challenge given the ever-increasing amount of HLWs and the shortage of long-term storage facilities.[1] With multiple approaches being discussed, an international consensus is that deep geological disposal is the preferred solution to the final management of HLW.[2] This technology is based on a combined natural and engineered multi-barrier system, where the host rock can efficiently retard the migration of hazardous radionuclides from the repository to the biosphere should a critical event happen. Because of the large time scale at concern, an important part of the design and performance assessment of underground HLW repositories is to predict the long-term evolution of the strongly coupled thermo-hydraulic-mechanical-chemical (THMC) processes in the clay buffers and the host rocks induced by material or energy release from the waste canisters. For example, the variation of pore pressure, water content, and elevated temperature could result in mechanical strain or even fractures in surrounding geomaterials.[3] In return, the skeleton deformation and fault displacement may alter the porosity and thus the permeability and diffusivity of the rock mass. Temperature change could be accelerated by fluid advection and chemical reaction. At the same time, heat transfer gives rise to thermal stresses and impacts mass transport of fluid as well as the reactive solute. Species migration is governed by concentration gradient but also influenced by fluid flow and thermal condition. Predicting the spatiotemporal evolution of such a complex environment near deep geological repositories requires reliable numerical models that can characterize all the relevant and highly nonlinear processes.[4]

To this end, considerable efforts have been devoted to developing solvers for the coupled nonlinear partial differential equations (PDEs) governing the THMC processes. Among the monolithic solvers, the OpenGeoSys (OGS) is an open-source numerical platform based on object-oriented finite element method (FEM), which is designed for multi-field problems of applications in geoscience and hydrology.[5-7] HYDROGEOCHEM is a suite of modules consisting of fluid flow, reactive biogeochemical transport, heat transfer and geomechanical displacement.[8] FEniCS is a popular and open-source computing framework that enables automated solution of PDEs with great flexibility and efficiency by a collection of FE-based libraries.[9] COMSOL Multiphysics is a commercial cross-platform finite element software and efficient solver for coupled PDEs, which has been successfully applied in THM(C) topics such as heat transfer in saturated soil,[10] methane hydrate[11] and CO_2 injection.[12] Apart from models that are solely based on FEM, the Los Alamos National Laboratory (LANL) has developed the Finite Element Heat and Mass Transfer (FEHM) code where the finite volume method (FVM) is utilized for flow and mass balance while FEM for stress equilibrium.[13] In addition, Feng et al.[14] proposed a method called the elasto-plastic cellular automaton (EPCA) which is inspired from

the self-organization theory and has been used to simulate the fracturing of novaculite in a THMC environment.[15] Solution of coupled problems can also be achieved by combining different codes in a staggered manner, permitting flexibility in software development. This includes schemes that integrate reactive flow simulation with geomechanics codes such as TOUGHREACT-FLAC3D[16-19] and TReactMech,[20, 21] or combining THM codes with geochemical simulator like MOOSE-REDBACK.[22] In general, sequential coupling approach has advantage on computational memory savings as well as implementation easiness. Whereas, solving coupled problems monolithically reduces communication and input/output (I/O) times compared to its staggered counterpart, which greatly benefits stability and avoids computational bottleneck.[13, 23] It is worth to note that some of the aforementioned codes are open-source while others are proprietary, and their detailed numerical procedures are seldom published in scientific journal papers. This often make it challenging for users especially beginners to modify or implement new coupled theories to accommodate for different materials and engineering systems.

This study reports the authors' independent effort to develop a fully implicit monolithic finite element solution for THMC problems, with special emphasis on full disclosure of the implementation and verification details as well as the source code. Particularly, all codes and scripts presented here are made openly accessible via the Supplementary Materials associated with this paper. We hope the details of the numerical procedure presented here can facilitate the numerical realization of other THMC or general multiphysical solvers. The FE software Abaqus Standard is chosen as the platform for our implementation considering its robust nonlinear solver that offers various implicit solution schemes as well as the automatic time-stepping capability. We start by outlining the general governing equations in Section 2. The thermoporoelasticity and the THM governing equations of Coussy[24] was adopted as the backbone of our THMC development. A user-defined element subroutine (UEL) is scripted in Section 3 based on the proposed governing equations. Considering the complexity of the system, the development starts by solving only the coupled hydromechanical equations, then extend to THM, and finally the complete THMC equations. Each implementation stage is verified by closed-form analytical solutions in Section 4. Finally, the UEL is put to simulate the in-situ heater test of ATLAS[25] in an underground research facility at Belgium (Section 5). The predicted THM responses of the host formation are evaluated against the measurement data from the experiment. A hypothetical leakage event is also simulated in the same FE model to examine the rate of contaminant migration through the host formation. The main conclusions of the study and possible future extensions are summarized in Section 6.

2. Governing equations

This section develops the governing equations describing the multiphysical processes in porous geological media based on the conservation of mass, momentum, and energy. The possible THMC processes in various host rocks has been discussed in several review papers and reports.[26] To establish a set of tangible governing equations in this initial development, we emphasize the strong coupling between THM and their weak coupling with C. Specifically, the C component will focus on the transport of contaminant species driven by concentration gradient and advection associated with bulk fluid flow (i.e., THM → C). It is known that the presence of active chemical species can alter the THM properties of the solid skeleton through adsorption,[27, 28] dissolution,[29] and pressure solution.[30] The system is also assumed to be fully saturated with no mass exchange between phases. This is likely to be true within the host rocks but not in the clay buffer where desaturation and vapor transportation may happen. These effects (i.e., C→THM) and phase changes may be included in future extensions of this basic framework. The main types of coupling considered in formulating the governing equations are summarized in Fig. 1. Based on these considerations, the set of unknown field variables are identified, including skeleton displacement (**u**), fluid pressure (P_f), temperature (T), and contaminant molar concentration (C).

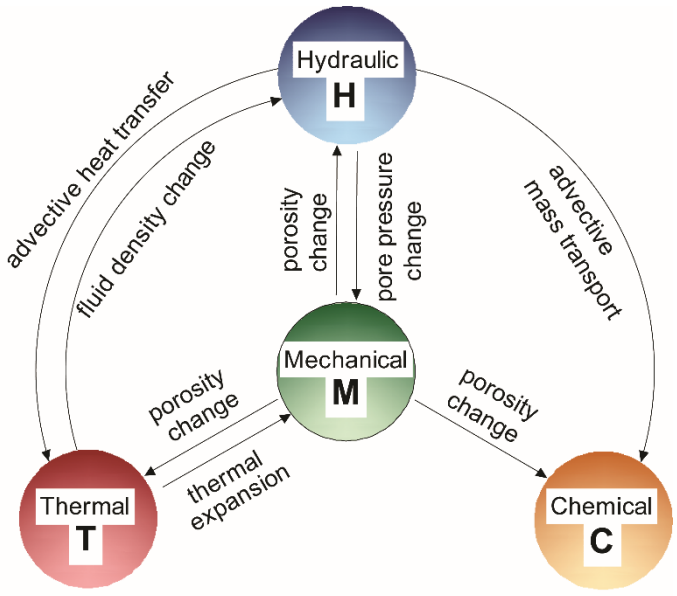

Fig. 1: THMC couplings considered in this study

2.1 Balance equation of mass and contaminant mole

A continuous description of a porous medium requires the analysis at macroscopic scale in accordance with the hypothesis of continuity.[24] Given an arbitrary domain with volume Ω_t and

boundary $\partial\Omega_t$, the rate of change of quantity ξ (e.g., mass density, molar concentration) in the α phase must be equal to the source/sink rate ; subtracts the net outflux with respect to the observing window. The conservation of ξ can be written in the following form:

$$\frac{D^{\alpha}}{Dt}\int_{\Omega_t}\xi d\Omega_t = \int_{\Omega_t}\frac{\partial\xi}{\partial t}d\Omega_t + \int_{\partial\Omega_t}\left(\xi\mathbf{v}_{\alpha}\right)\cdot\mathbf{n}da = \int_{\Omega_t} \quad (1)$$

where

$$\frac{D^{\alpha}}{Dt}(\cdot) = \frac{\partial}{\partial t}(\cdot) + \mathbf{v}_{\alpha}\cdot\nabla_x(\cdot)$$

is the particle derivative with respect to the α phase; Ω_t is the domain volume; *da* is a unit domain boundary; $\mathbf{v}_{\alpha}$ is the velocity of the α phase; $\nabla_x(\cdot)$ denotes gradient operation with respect to spatial coordinate; $\alpha = s$ for solid and f for fluid in this development. As discussed previously, mass or species exchanges between phases are neglected in this study and thus . After applying divergence theorem, Equation (1) can be written in local form as:

$$\frac{\partial\xi}{\partial t} + \nabla_x\cdot\left(\xi\mathbf{v}_{\alpha}\right) = 0 \quad (2)$$

This equation is expressed in relation to a spatially fixed observation window. For FE implementation, governing equations often need to be expressed with respect to a window that moves along with the solid skeleton. Equation (2) can be thus re-written as

$$\frac{D^{s}}{Dt}(\xi) + \xi\nabla_x\cdot\mathbf{v}_s + \nabla_x\cdot\left[\left(\mathbf{v}_{\alpha}-\mathbf{v}_s\right)\xi\right] = 0 \quad (3)$$

Let ξ be the fluid mass per unit total volume ($n\rho_f$), where n is the Eulerian porosity and ρ_f is the intrinsic density of the fluid. The fluid mass balance can be written based on Equation (3) as:

$$\rho_f\frac{D^{s}n}{Dt} + n\frac{D^{s}\rho_f}{Dt} + n\rho_f\nabla_x\cdot\mathbf{v}_s + \nabla_x\cdot\mathbf{q}_f = 0 \quad (4)$$

where $\mathbf{q}_f$ is the relative flow vector of fluid mass:

$$\mathbf{q}_f = n\rho_f\left(\mathbf{v}_f - \mathbf{v}_s\right) \quad (5)$$

Similarly, the solid mass balance can be established by letting ξ be the solid mass per unit total volume $(1-n)\rho_s$:

$$-\rho_s\frac{D^{s}n}{Dt} + (1-n)\frac{D^{s}\rho_s}{Dt} + (1-n)\rho_s\nabla_x\cdot\mathbf{v}_s = 0 \quad (6)$$

where ρ_s is the intrinsic density of the solid. Set ξ as the contaminant molar concentration nC where C is amount of moles per unit fluid volume. The mole conservation equation for any contaminant species can be similarly written as:

$$\frac{D^s}{Dt}(nC)+nC\nabla_x\cdot\mathbf{v}_s+\nabla_x\cdot\left[\left(\mathbf{v}_C-\mathbf{v}_s\right)nC\right]=0 \tag{7}$$

Define molar flux vector of contaminant relative to the bulk fluid flow

$$\mathbf{q}_C=nC\left(\mathbf{v}_C-\mathbf{v}_f\right) \tag{8}$$

Equation (7) can then be rewritten as

$$n\frac{D^sC}{Dt}+C\frac{D^sn}{Dt}+Cn\nabla_x\cdot\mathbf{v}_s+\nabla_x\cdot\left(\frac{C}{\rho_f}\mathbf{q}_f\right)+\nabla_x\cdot\mathbf{q}_C=0 \tag{9}$$

2.2 Mechanical equilibrium

The balance of linear momentum of porous domain Ω_t can be written as

$$\frac{D^s}{Dt}\int_{\Omega_t}\rho_s\left(1-n\right)\mathbf{v}_s d\Omega_t+\frac{D^f}{Dt}\int_{\Omega_t}\rho_f n\mathbf{v}_f d\Omega_t=\int_{\Omega_t}\mathbf{b}d\Omega_t+\int_{\partial\Omega_t}\boldsymbol{\sigma}\cdot\mathbf{n}da \tag{10}$$

where $\boldsymbol{\sigma}$ is the Cauchy stress tensor; $\mathbf{b}$ is the body force per unit volume that only includes gravitational force in this model (i.e. $\mathbf{b}=[n\rho_f+(1-n)\rho_s]\mathbf{g}$). Equation (10) can be further written in local form by considering Reynold transport theorem and mass balance for solid and fluid phases:

$$\left[\rho_s\left(1-n\right)\right]\boldsymbol{\gamma}_s+\left(\rho_f n\right)\boldsymbol{\gamma}_f=\nabla_x\cdot\boldsymbol{\sigma}+\mathbf{b} \tag{11}$$

where $\boldsymbol{\gamma}_\alpha$ is the acceleration vector of phase α=*s* or *f*. Under quasi-static condition which is of the current interest, all the inertia terms can be neglected and the equilibrium equation becomes

$$\nabla_x\cdot\boldsymbol{\sigma}+\mathbf{b}=0 \tag{12}$$

2.3 Balance equation of internal energy

For fine-grained porous media, local thermal equilibrium is a reasonable assumption considering the rapid conduction between the fluid and the solid phases.[12] This means a single value *T* can be used to represent the absolute temperature of all phases in the representative element volume (REV). Neglecting the mechanical work, the balance of internal energy of the system can be written as

$$\begin{aligned}&\frac{D^s}{Dt}\int_{\Omega_t}\left[\left(1-n\right)\rho_s c_s T+n\rho_f c_f T\right]dV\\&=-\int_{\partial\Omega_t}n\rho_f c_f T\left(\mathbf{v}_f-\mathbf{v}_s\right)\cdot\mathbf{n}dA-\int_{\partial\Omega_t}\mathbf{q}_T\cdot\mathbf{n}dA+\int_{\Omega_t}\end{aligned} \tag{13}$$

where c_α is the specific heat of phase α; the first term on the right-hand side (RHS) accounts for the advective energy flux due to fluid escaping on the domain boundary; $\mathbf{q}_T$ is the rate of heat flux due to thermal conduction. Applying the Reynold transport theorem and divergence theorem and setting , the local form of energy balance can be written as:

$$\frac{\partial\left[\left(1-n\right)\rho_s c_s T+n\rho_f c_f T\right]}{\partial t}+\nabla_x\cdot\left(1-n\right)\rho_s c_s T\mathbf{v}_s+\nabla_x\cdot n\rho_f c_f T\mathbf{v}_f+\nabla_x\cdot\mathbf{q}_T=0 \tag{14}$$

or

$$\frac{D^s}{Dt}\left[\left(1-n\right)\rho_s c_s T+n\rho_f c_f T\right]+\left[\left(1-n\right)\rho_s c_s T+n\rho_f c_f T\right]\nabla_x\cdot\mathbf{v}_s+\nabla_x\cdot c_f T\mathbf{q}_f+\nabla_x\cdot\mathbf{q}_T=0 \tag{15}$$

Assuming c_s and c_f are constant, Equation (15) can be finally expanded as:

$$\begin{aligned}&\left[\left(1-n\right)\rho_s c_s+n\rho_f c_f\right]\frac{D^s T}{Dt}\\&+T\left[c_s\rho_s\frac{D^s\left(1-n\right)}{Dt}+c_s\left(1-n\right)\frac{D^s\rho_s}{Dt}+c_f\rho_f\frac{D^s n}{Dt}+c_f n\frac{D^s\rho_f}{Dt}\right]\\&+\left[\left(1-n\right)\rho_s c_s T+n\rho_f c_f T\right]\nabla_x\cdot\mathbf{v}_s+\nabla_x\cdot c_f T\mathbf{q}_f+\nabla_x\cdot\mathbf{q}_T=0\end{aligned} \tag{16}$$

2.4 Constitutive relation and conduction laws

At material level, we need to specify 1) a constitutive relation to describe the mechanical behavior of the REV under stress, fluid pressure, and temperature variation, and 2) a set of conduction laws to describe fluid flow, contaminant transport and heat transfer under their driving gradients. The material model shall be implemented in a hierarchical way such that different types of constitutive laws which may be nonlinear, inelastic, and anisotropic can be easily accommodated. This will be discussed in the next section. To have a starting point, we choose the thermoporoelastic theory by Coussy[24] as the constitutive model. The expression of this model in terms of infinitesimal strain is given by:

$$\sigma_{ij}-\sigma_{ij,0}=C_{ijkl}\varepsilon_{kl}-b_{ij}\left(P_f-P_{f,0}\right)-C_{ijkl}\alpha_{kl}\left(T-T_0\right) \tag{17}$$

$$\phi-\phi_0=b_{ij}\varepsilon_{ij}+\frac{P_f-P_{f,0}}{N}-3\alpha_\phi\left(T-T_0\right) \tag{18}$$

where

$$\boldsymbol{\varepsilon}=\frac{1}{2}\left(\nabla\mathbf{u}+\nabla\mathbf{u}^T\right) \tag{19}$$

is the infinitesimal strain tensor; ϕ the Lagrangian porosity; b_{ij} the Biot's coefficient; α_{kl} the thermal expansion coefficient of the solid; N the Biot's tangent modulus linking pressure and porosity changes; $3\alpha_\phi$ the volumetric thermal dilation coefficient related with porosity; C_{ijkl} the stiffness matrix of the skeleton; $\sigma_{ij,0}$, $P_{f,0}$, T_0 and ϕ_0 characterize the reference initial state of the specimen. Equations (17) and (18) can be further simplified by assuming linear isotropic elastic response and isotropic thermal expansion coefficient. Additionally, a conversion between porosity ϕ to n is necessary to maintain consistency with the field equations. Under infinitesimal strain condition, we

have $\phi = Jn \approx (1+\varepsilon_v)n$ according to Coussy[24]. The relation between the increments of the two porosity measures can be derived as:

$$d\phi \approx dn + \varepsilon_v dn + n d\varepsilon_v \approx dn + n d\varepsilon_v \tag{20}$$

where $\varepsilon_v dn$ is neglected because it is a second-order infinitesimal term. Considering the above, Equations (17) and (18) can be simplified to:

$$\sigma_{ij} - \sigma_{ij,0} = \left(K - \frac{2}{3}G\right)\varepsilon_v \delta_{ij} + 2G\varepsilon_{ij} - b\left(P_f - P_{f,0}\right)\delta_{ij} - 3\alpha K\left(T - T_0\right)\delta_{ij} \tag{21}$$

$$n - n_0 = (b-n)\varepsilon_v + \frac{P_f - P_{f,0}}{N} - 3\alpha_\phi\left(T - T_0\right) \tag{22}$$

where *K* is the bulk modulus and *G* is the shear modulus; *b* and *α* the isotropic Biot's coefficient and thermal expansion coefficient, respectively; $\varepsilon_v = \varepsilon_{ii}$ the volumetric strain; δ_{ij} the Kronecker delta. Equations (21) and (22) can be rewritten in incremental matrix form for numerical implementation:

$$\begin{bmatrix} d\sigma_{11} \\ d\sigma_{22} \\ d\sigma_{33} \\ d\sigma_{23} \\ d\sigma_{13} \\ d\sigma_{12} \\ dn \end{bmatrix} = \begin{bmatrix} K+\frac{4}{3}G & K-\frac{2}{3}G & K-\frac{2}{3}G & 0 & 0 & 0 & -b & -3\alpha K \\ K-\frac{2}{3}G & K+\frac{4}{3}G & K-\frac{2}{3}G & 0 & 0 & 0 & -b & -3\alpha K \\ K-\frac{2}{3}G & K-\frac{2}{3}G & K+\frac{4}{3}G & 0 & 0 & 0 & -b & -3\alpha K \\ 0 & 0 & 0 & 2G & 0 & 0 & 0 & 0 \\ 0 & 0 & 0 & 0 & 2G & 0 & 0 & 0 \\ 0 & 0 & 0 & 0 & 0 & 2G & 0 & 0 \\ b-n & b-n & b-n & 0 & 0 & 0 & \frac{1}{N} & -3\alpha_\phi \end{bmatrix} \begin{bmatrix} d\varepsilon_{11} \\ d\varepsilon_{22} \\ d\varepsilon_{33} \\ d\varepsilon_{23} \\ d\varepsilon_{13} \\ d\varepsilon_{12} \\ dP_f \\ dT \end{bmatrix} \tag{23}$$

Regarding the conduction laws, it is possible to write a general linear conduction law:

$$\begin{bmatrix} \mathbf{q}_f \\ \mathbf{q}_T \\ \mathbf{q}_C \end{bmatrix} = -\begin{bmatrix} \mathbf{k}_{HH} & \mathbf{k}_{HT} & \mathbf{k}_{HC} \\ \mathbf{k}_{TH} & \mathbf{k}_{TT} & \mathbf{k}_{TC} \\ \mathbf{k}_{CH} & \mathbf{k}_{CT} & \mathbf{k}_{CC} \end{bmatrix} \begin{bmatrix} \nabla P_f - \rho_f \mathbf{g} \\ \nabla T \\ \nabla C \end{bmatrix} \tag{24}$$

The simplest conduction law controls fluid flow is the Darcy's law which states a linear relation between $\mathbf{q}_f$ and ∇P_f :

$$\mathbf{q}_f = -\frac{\rho_f k}{\mu}\left(\nabla_x P_f - \rho_f \mathbf{g}\right) \tag{25}$$

where *k* is the permeability and *μ* is the dynamic viscosity of the fluid. Similarly, the contaminant diffusion and heat conduction are classically described by the Fick's and the Fourier's law, respectively:

$$\mathbf{q}_C = -D_C \nabla_x C \tag{26}$$

$$\mathbf{q}_T = -\kappa \nabla_x T \tag{27}$$

where D_C is the diffusivity of contaminant species; κ is the thermal diffusivity. The diffusion coefficients k, D_C and κ are scalars for isotropic solid, which is what we have assumed here. Neglecting the coupling terms, the simplest form of Equation (24) can be written by collecting Equations (25) - (27):

$$\begin{bmatrix} \mathbf{q}_f \\ \mathbf{q}_T \\ \mathbf{q}_C \end{bmatrix} = -\begin{bmatrix} \rho_f k/\mu & 0 & 0 \\ 0 & \kappa & 0 \\ 0 & 0 & D_C \end{bmatrix} \begin{bmatrix} \nabla_x P_f - \rho_f \mathbf{g} \\ \nabla_x T \\ \nabla_x C \end{bmatrix} \tag{28}$$

2.5 Equation of state

Finally, the compressibility of the fluid and the solid phases needs to be defined to close the system. Assuming the intrinsic fluid density is a function of pore pressure P_f and temperature T, the equation of state for the fluid phase can be written as

$$d\rho_f = \frac{\partial \rho_f}{\partial P_f} dP_f + \frac{\partial \rho_f}{\partial T} dT = \frac{\rho_f}{K^f} dP_f - 3\rho_f \alpha_f dT \tag{29}$$

where $3\alpha_f$ is the coefficient of volumetric thermal expansion of the fluid; K^f is fluid bulk modulus. For the solid phase, combining solid mass balance Equation (6) and the porosity evolution law Equation (22) gives

$$d\rho_s = \frac{-\rho_s}{1-n}\left[(1-b)\, d\varepsilon_v - \frac{dP_f}{N} + 3\alpha_\phi dT\right] \tag{30}$$

After supplying Equations (29) and (30), the final THMC governing equations are derived and summarized in Table 1. For conciseness, the operator $D^s\xi/Dt$ is replaced by superposed dot $\dot{\xi}$; the spatial gradient ∇_x is replaced by ∇; $\nabla \cdot \mathbf{v}_s$ is essentially the volumetric strain rate $\dot{\varepsilon}$. The key assumptions behind the equations in Table 1 are: 1) The host rock under consideration is fully saturated, linear elastic, with compressible constituents undergoing small deformations, whereas plasticity, damage, or partial saturation of the rock are not considered; 2) The effect of stress and temperature on the transport coefficients (e.g., permeability, diffusivity) are neglected; 3) The effects of fluid chemistry on the THM properties of the host rock through processes such as adsorption, dissolution, and pressure solution (i.e., C→THM) are omitted. The system is to be solved by the finite element method, complemented by constitutive relation Equation (23) and conduction law Equation (28).

3. Finite element implementation

In this section, the governing equations are spatially and temporally discretized and solved under an iterative scheme through the user-define element (UEL) subroutine combined with Abaqus Standard. It should be acknowledged that this development mainly follows the UEL implementation of a coupled diffusion-deformation theory for elastomeric gels by Chester et al.[31].

3.1 The structure of UEL

The UEL subroutine permits user-defined variational form of the elemental Jacobian (or tangent stiffness) matrix (AMATRX) and the residual vector (RHS) in solving customized equation systems. We choose to use a three-dimensional trilinear hexahedron element (U3D8) with 6 degrees of freedom (DOFs) which are respectively u_x, u_y, u_z, P_f, C and T for each node (See Appendix, Fig. A). Admittedly, this type of element do not satisfy the Ladyzhenskaya–Babuska–Brezzi (LBB) condition[32, 33] and can give unphysical oscillation in the results. Multiple techniques have been developed to avoid such spurious pressure mode.[23, 34, 35] Considering these oscillations are short-lived and do not impair the equilibrium or the long-term solution of interest to this study, we opt for the basic low-order element type in this first-stage development. Similar approach is also adopted in other coupled deformation-diffusion UEL codes.[31]

The proposed UEL is hierarchically structured so that it does not contain any constitutive information of the material. Instead, the UEL will call a separate *Material* subroutine at material integration points to retrieve the constitutive relations. The advantage of doing so is to have the versatility to switch to advanced material models should the nonlinear, inelastic, and anisotropic responses of different rock formations be incorporated in the future. The workflow is sketched in Fig. 2. At the starting point, nodal coordinates (COORDS), estimated DOFs for next step (U), and material parameters defined in an input file (PROPS) are passed from Abaqus to the UEL. After interpolation from nodal values, this information computes the RHS and AMATRX at each Gauss point, which will be upscaled to the element level through Gauss quadrature. In addition, all solution dependent variables (SVARS) are updated and stored at the end of each iteration.[36] Whenever the UEL is called, it returns the elemental RHS and AMATRX which will be later assembled for the global Newton-Raphson iteration in the Abaqus Standard solver. If the global RHS meets the desired tolerance, we say the system reaches convergence and the PDEs are numerically solved.

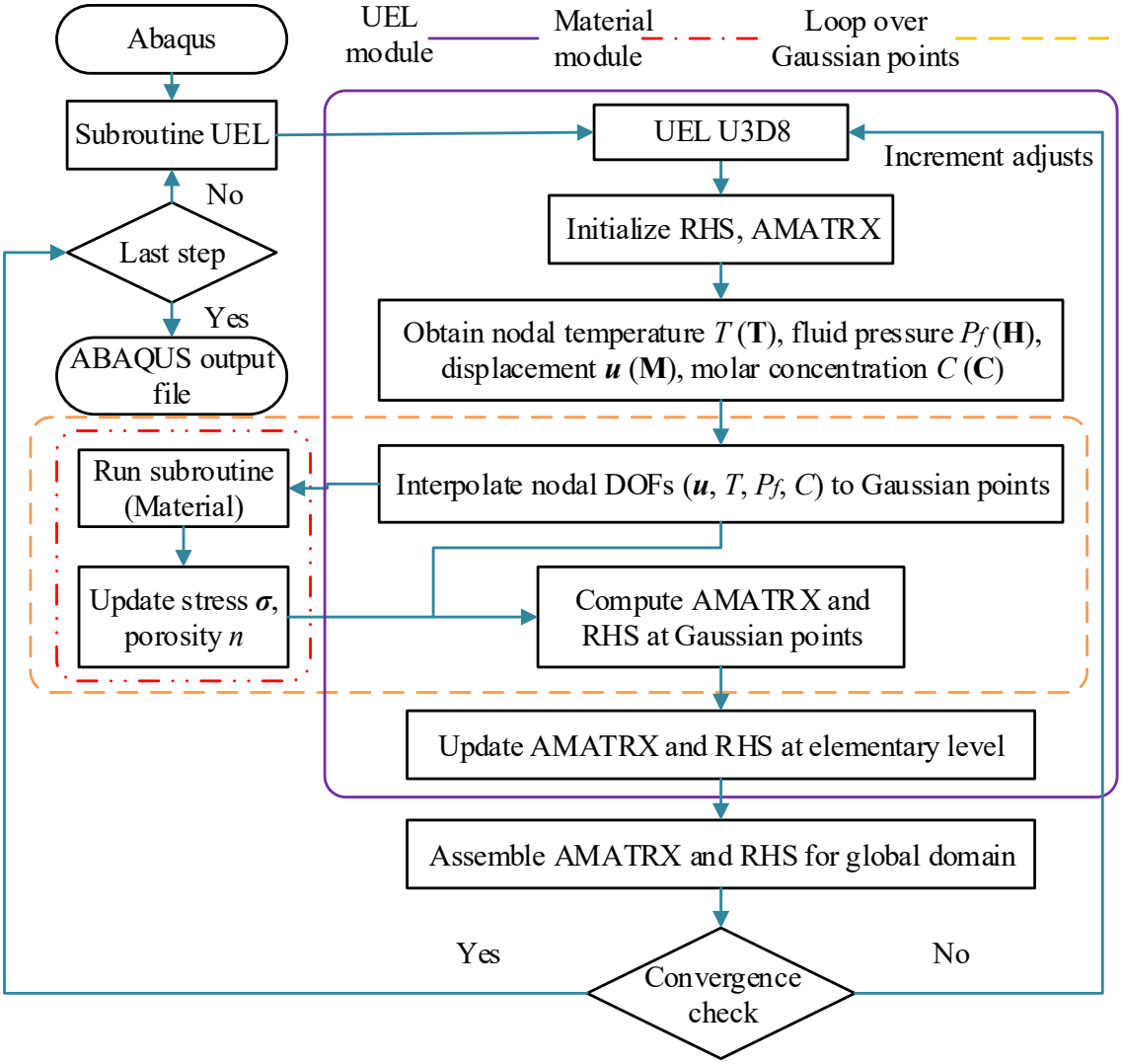

Fig. 2: Workflow of THMC modeling via Abaqus + UEL

Visualization of the computed results is not straightforward as Abaqus cannot automatically extrapolate variables from Gauss points to nodes for user-customized shape functions. This can be addressed by coding a python script that accesses the output database and translates the data format to be compatible with other third-party post-processing software.[37] Here a convenient approach that only involves Abaqus CAE is adopted: each user-defined element is overlaid by an Abaqus built-in element (also called the dummy element) which has the identical shape function as the UEL. The material-point quantities computed from the UEL are passed to the dummy element via subroutine UVARM, which can then be understood and visualized by Abaqus CAE. To avoid interferences with the FE computations, all dummy elements must be assigned with near-zero stiffness and T/H/C conductivity coefficients.

3.2 Boundary and initial conditions

The definition of boundary and initial conditions are required to complete the formulation of IBVP given a time interval $t \in [0,T]$. For a domain Ω with boundary Γ=∂Ω, let Γ_β^D and Γ_β^N be a pair of complementary subsurface where the Dirichlet and Neumann boundary conditions are prescribed respectively for the *β* field (*β*=M, H, C, T), following the relation that $\Gamma = \Gamma_\beta^D \cup \Gamma_\beta^N$ and $\Gamma_\beta^D \cap \Gamma_\beta^N = \varnothing$. Therefore, the formal statement of initial and boundary conditions for the fully coupled THMC system are as follows:

$$\text{M(mechanical)}: \begin{Bmatrix} \mathbf{u}(\mathbf{x},0) = \mathbf{u}_0(\mathbf{x}) \\ \mathbf{u} = \breve{\mathbf{u}} \qquad \forall \mathbf{x} \in \Gamma_M^D \\ \boldsymbol{\sigma}\mathbf{n} = \breve{\mathbf{t}} \qquad \forall \mathbf{x} \in \Gamma_M^N \end{Bmatrix} \tag{31}$$

$$\text{H(hydraulic)}: \begin{Bmatrix} P_f(\mathbf{x},0) = P_{f,0}(\mathbf{x}) \quad n(\mathbf{x},0) = n_0(\mathbf{x}) \\ P_f = \breve{P}_f \qquad \forall \mathbf{x} \in \Gamma_H^D \\ \mathbf{q}_f\mathbf{n} = \breve{q}_f \qquad \forall \mathbf{x} \in \Gamma_H^N \end{Bmatrix} \tag{32}$$

$$\text{C(chemical)}: \begin{Bmatrix} C(\mathbf{x},0) = C_0(\mathbf{x}) \\ C = \breve{C} \qquad \forall \mathbf{x} \in \Gamma_C^D \\ \mathbf{q}_C\mathbf{n} = \breve{q}_C \qquad \Gamma_C^N \\ C\mathbf{q}_f\mathbf{n} = \breve{q}_{C,f} \qquad \forall \mathbf{x} \in \Gamma_{C,H}^N \end{Bmatrix} \tag{33}$$

$$\text{T(thermal)}: \begin{Bmatrix} T(\mathbf{x},0) = T_0(\mathbf{x}) \\ T = \breve{T} \qquad \forall \mathbf{x} \in \Gamma_T^D \\ \mathbf{q}_T\mathbf{n} = \breve{q}_T \qquad \forall \mathbf{x} \in \Gamma_T^N \\ c_f T\mathbf{q}_f\mathbf{n} = \breve{q}_{T,f} \qquad \forall \mathbf{x} \in \Gamma_{T,H}^N \end{Bmatrix} \tag{34}$$

3.3 Weak form and discretization

We shall now construct the weak form of the THMC problem by multiplying the residual with a set weight functions $\mathbf{w}_1$, w_2, w_3, w_4 and integrating over the whole domain for solving the unknowns ***u***, P_f, *C*, *T*, respectively. In terms of integral forms for weighted residuals, trial functions for solution approximation must be selected from a Sobolev space H^m (of order *m*) with the embedded Dirichlet boundary conditions. Likewise, weight functions ($\mathbf{w}_1$, w_2, w_3, w_4) are selected from Sobolev space with the same continuity and differentiability requirements but will vanish on the Dirichlet boundaries. Combining those derivation of integrating products, definition for weight and trial functions, and Neumann boundary conditions defined in Equations (31) - (34), the weak forms are stated as follows:

$$\text{M:}\left\{\begin{array}{c}\int_\Omega \nabla_s{}^T \mathbf{w}_1 \boldsymbol{\sigma} d\Omega = \mathbf{w}_1 \text{[illegible]} \int_\Omega \mathbf{w}_1 \text{[illegible]} n\rho_f + (1-n)\rho_s \big] \mathbf{g} d\Omega \\ \mathbf{u} \in H^1(\Omega):\ \mathbf{u} = \text{[illegible]} \quad \text{[illegible]} \ \Gamma_M^D \\ \mathbf{w}_1 \in H^1(\Omega):\ \mathbf{w}_1 = 0 \ \forall \mathbf{x} \in \Gamma_M^D \end{array}\right\} \tag{35}$$

$$\text{H:}\left\{\begin{array}{c}\int_\Omega w_2 \rho_f \text{[illegible]} \quad \text{[illegible]} \ n\big(\rho_f \text{[illegible]} \\ + w_2 n \rho_f \text{[illegible]} \quad \text{[illegible]} \int_\Omega \text{[illegible]} \cdot \nabla w_2 d\Omega = 0 \\ P_f \in H^1(\Omega):\ P_f = \text{[illegible]} \quad \forall \mathbf{x} \in \Gamma_H^D \\ w_2 \in H^1(\Omega):\ \mathrm{w}_2 = 0 \quad \forall \mathbf{x} \in \Gamma_H^D \end{array}\right\} \tag{36}$$

$$\text{C:}\left\{\begin{array}{c}\int_\Omega w_3 n \text{[illegible]} \quad \text{[illegible]} \ C \text{[illegible]} \quad \text{[illegible]} \ (Cn) \text{[illegible]} \\ + w_3 \text{[illegible]} \int_\Omega \text{[illegible]} \quad \int_\Omega \text{[illegible]} \\ C \in H^1(\Omega):\ C = \text{[illegible]} \quad \forall \mathbf{x} \in \Gamma_C^D \\ w_3 \in H^1(\Omega):\ \mathrm{w}_3 = 0 \quad \forall \mathbf{x} \in \Gamma_C^D \end{array}\right\} \tag{37}$$

$$\text{T:}\left\{\begin{array}{c}\int_\Omega w_4 \left\{\begin{array}{l}\big[(1-n)\rho_s c_s + n\rho_f c_f\big] \text{[illegible]} \\ + T\big(c_f \rho_f - c_s \rho_s\big) \text{[illegible]} \quad \text{[illegible]} \\ + \big[(1-n)\rho_s c_s T + n\rho_f c_f T\big] \text{[illegible]} \end{array}\right\} d\Omega \\ + w_4 c_f T \text{[illegible]} \quad \int_\Omega \text{[illegible]} \quad \text{[illegible]} \quad 0 \\ T \in H^1(\Omega):\ T = \text{[illegible]} \quad \forall \mathbf{x} \in \Gamma_T^D \\ w_4 \in H^1(\Omega):\ \mathrm{w}_4 = 0 \quad \forall \mathbf{x} \in \Gamma_T^D \end{array}\right\} \tag{38}$$

The finite element formulation is established by applying the Bubnov-Galerkin method, where the solution can be approximated by using the identical shape function **N** for trial and weight functions, namely:

M: with $\mathbf{u} = \mathbf{N}$ [illegible] and $\mathbf{w}_1 = \mathbf{N}$ [illegible]

$$\int_\Omega \mathbf{B}^T \boldsymbol{\sigma}(\mathbf{u}) d\Omega - \mathbf{N}^T \text{[illegible]} \quad \int_\Omega \text{[illegible]} \big[n\rho_f + (1-n)\rho_s\big] \mathbf{g} d\Omega = 0 \tag{39}$$

H: with $P_f = \mathbf{N}$ [illegible] and $w_2 = \mathbf{N}$ [illegible]

$$\begin{array}{l}\int_\Omega \mathbf{N}^T \rho_f \text{[illegible]} \quad \mathbf{N}^T n\big(\rho_f / K^f \text{[illegible]} \\ + \int_\Omega \mathbf{N}^T n \rho_f \text{[illegible]} \quad \text{[illegible]} \quad \int_\Omega \text{[illegible]} \mathbf{N}\big)^T \mathbf{q}_f d\Omega = 0 \end{array} \tag{40}$$

C: with $C = \mathbf{N}$ [illegible] and $w_3 = \mathbf{N}$ [illegible]

$$\mathbf{N}^T n\dot{\quad} \quad \mathbf{N}^T C\dot{\quad} \quad \mathbf{N}^T (Cn)\dot{\quad}$$
$$+\mathbf{N}^T \breve{q}_{c,f} \quad \int_\Omega \quad \int_\Omega \quad \breve{q}_c \quad \int_\Omega \quad (41)$$

T: with $T = \mathbf{N}\breve{T}$ and $w_4 = \mathbf{N}\breve{w}_4$

$$\int_\Omega \mathbf{N}^T \left[(1-n)\rho_s c_s + n\rho_f c_f\right] \dot{T}$$
$$+\int_\Omega \mathbf{N}^T T\left(c_f \rho_f - c_s \rho_s\right)\dot{n} \quad \mathbf{N}^T T c_f n \rho_f \left(\dot{T}\right.$$
$$+\int_\Omega \mathbf{N}^T \left[(1-n)\rho_s c_s + n\rho_f c_f\right] T\dot{\quad} \quad (42)$$
$$+\mathbf{N}^T c_f \breve{q}_{T,f} \quad \int_\Omega \quad \breve{q}_T \quad \int_\Omega \quad)$$

where

$$\mathbf{B} = \nabla_s \mathbf{N} = \begin{bmatrix} \frac{\partial N_1}{\partial x} & 0 & 0 & \frac{\partial N_2}{\partial x} & 0 & 0 & \dots & \frac{\partial N_n}{\partial x} & 0 & 0 \\ 0 & \frac{\partial N_1}{\partial y} & 0 & 0 & \frac{\partial N_2}{\partial y} & 0 & \dots & 0 & \frac{\partial N_n}{\partial y} & 0 \\ 0 & 0 & \frac{\partial N_1}{\partial z} & 0 & 0 & \frac{\partial N_2}{\partial z} & \dots & 0 & 0 & \frac{\partial N_n}{\partial z} \\ 0 & \frac{\partial N_1}{\partial z} & \frac{\partial N_1}{\partial y} & 0 & \frac{\partial N_2}{\partial z} & \frac{\partial N_2}{\partial y} & \dots & 0 & \frac{\partial N_n}{\partial z} & \frac{\partial N_n}{\partial y} \\ \frac{\partial N_1}{\partial z} & 0 & \frac{\partial N_1}{\partial x} & \frac{\partial N_2}{\partial z} & 0 & \frac{\partial N_1}{\partial x} & \dots & \frac{\partial N_n}{\partial z} & 0 & \frac{\partial N_n}{\partial x} \\ \frac{\partial N_1}{\partial y} & \frac{\partial N_1}{\partial x} & 0 & \frac{\partial N_2}{\partial y} & \frac{\partial N_1}{\partial x} & 0 & \dots & \frac{\partial N_n}{\partial y} & \frac{\partial N_n}{\partial x} & 0 \end{bmatrix} \quad (43)$$

More details about the element type and expanded shape function are presented in Appendix A.

3.4 UEL implementation

During each iteration attempt, the elemental Jacobian **K**=AMATRX and the residual **R**=RHS must be evaluated to solve all nodal unknowns $\breve{\delta}$ via:

$$\mathbf{K}\breve{\delta}$$

or

$$\underbrace{\begin{bmatrix} \mathbf{K}_{uu}^{t+\Delta t} & \mathbf{K}_{uP}^{t+\Delta t} & \mathbf{K}_{uC}^{t+\Delta t} & \mathbf{K}_{uT}^{t+\Delta t} \\ 3n_e \times 3n_e & 3n_e \times n_e & 3n_e \times n_e & 3n_e \times n_e \\ \mathbf{K}_{Pu}^{t+\Delta t} & \mathbf{K}_{PP}^{t+\Delta t} & \mathbf{K}_{PC}^{t+\Delta t} & \mathbf{K}_{PT}^{t+\Delta t} \\ n_e \times 3n_e & n_e \times n_e & n_e \times n_e & n_e \times n_e \\ \mathbf{K}_{Cu}^{t+\Delta t} & \mathbf{K}_{CP}^{t+\Delta t} & \mathbf{K}_{CC}^{t+\Delta t} & \mathbf{K}_{CT}^{t+\Delta t} \\ n_e \times 3n_e & n_e \times n_e & n_e \times n_e & n_e \times n_e \\ \mathbf{K}_{Tu}^{t+\Delta t} & \mathbf{K}_{TP}^{t+\Delta t} & \mathbf{K}_{TC}^{t+\Delta t} & \mathbf{K}_{TT}^{t+\Delta t} \end{bmatrix}}_{\text{AMATRX}} \underbrace{\begin{bmatrix} \breve{\delta} \\ 3n_e \\ \breve{\delta}_f \\ n_e \\ \breve{\delta} \\ n_e \\ \breve{\delta}_T \end{bmatrix}}_{\text{RHS}} \quad (44)$$

where n_e is the number of nodes which equals to 8 for the current element type U3D8. According to Equations (39) - (42), the residual $\mathbf{R}$ at $t+\Delta t$ step is given below:

$$\mathbf{R}_{\mathbf{M}}^{t+\Delta t} = -\int_{\Omega}\mathbf{B}^T\boldsymbol{\sigma}^{t+\Delta t}d\Omega - \mathbf{N}^T\breve{\mathbf{t}}\int_{\Omega^1}\left[n^{t+\Delta t}\rho_f + \left(1-n^{t+\Delta t}\right)\rho_s\right]\mathbf{g}d\Omega \tag{45}$$

$$\begin{aligned} R_H^{t+\Delta t} &= -\int_{\Omega}\mathbf{N}^T\rho_f\dot{} \qquad \mathbf{N}^T n\left(\rho_f\dot{}\right.\\ &-\frac{1}{\Delta t}\int_{\Omega}\mathbf{N}^T n^{t+\Delta t}\rho_f\dot{} \qquad \int_f^k\mathbf{N}^T\breve{\mathbf{q}}_f\cdots\int_{\Omega}(\nabla\mathbf{N})^T\mathbf{q}_f^{t+\Delta t}d\Omega \end{aligned} \tag{46}$$

$$\begin{aligned} R_C^{t+\Delta t} &= -\int_{\Omega}\mathbf{N}^T n^{t+\Delta t}\dot{} \qquad \mathbf{N}^T C^{t+\Delta t}\dot{} \qquad \mathbf{N}^T\left(C^{t+\Delta t}n^{t+\Delta t}\right)\dot{}\\ &-\mathbf{N}^T\breve{\mathbf{q}}_{C,f}\cdots + \int_{\Omega}\left(C^{t+\Delta t}\mathbf{q}_f^{t+\Delta t}/\rho_f\right)\cdot\nabla\mathbf{N}d\Omega - \mathbf{N}^T\breve{\mathbf{q}}_C\cdots\int_{\Omega}\mathbf{q}_C^{t+\Delta t}\cdot\nabla\mathbf{N}d\Omega \end{aligned} \tag{47}$$

$$\begin{aligned} R_T^{t+\Delta t} &= -\int_{\Omega}\mathbf{N}^T\left[\left(1-n^{t+\Delta t}\right)\rho_s c_s + n^{t+\Delta t}\rho_f c_f\right]\dot{}\\ &+\int_{\Omega}\mathbf{N}^T T^{t+\Delta t}c_s\rho_s\left[(1-b)\dot{}\right.\\ &-\int_{\Omega}\mathbf{N}^T T^{t+\Delta}\left(c_f\rho_f - c_s\rho_s\right)\dot{} \qquad \mathbf{N}^T T^{t+\Delta t}c_f n^{t+\Delta t}\rho_f\left(\dot{}\right.\\ &-\frac{1}{\Delta t}\int_{\Omega}\mathbf{N}^T\left[\left(1-n^{t+\Delta t}\right)\rho_s c_s + n^{t+\Delta t}\rho_f c_f\right]T^{t+\Delta t}\dot{} \qquad c_f\breve{\mathbf{q}}_{T,f}\\ &+\int_{\Omega}\left(c_f T^{t+\Delta t}\mathbf{q}_f^{t+\Delta t}\right)\cdot\nabla\mathbf{N}d\Omega - \mathbf{N}^T\breve{\mathbf{q}}_T\cdots\int_{\Omega}\mathbf{q}_T^{t+\Delta t}\cdot\nabla\mathbf{N}d\Omega \end{aligned} \tag{48}$$

To explicitly write the Jacobian matrix, the derivatives of residuals ($\mathbf{R_M}$, R_H, R_C, R_T) with respect to increments of unknown variables ($\delta\breve{\ }$, $\delta\breve{\ }_f$, $\delta\breve{C}$, $\delta\breve{\ }$) must be derived. The accuracy of the derived Jacobian **K** will determine the convergence performance of the global iteration thus influencing the computation efficiency especially in some highly nonlinear problems.[38] Therefore, great care was taken in deriving the Jacobian for the THMC system here. Note that **R** and **K** matrixes contain many definite integral terms over the element. One needs to evaluate these integrals by Gaussian quadrature after mapping them from global coordinates (*x, y, z*) to local reference coordinates (*ξ*, *η*, *ζ*) under the isoparametric element scheme. The final expressions of **R** and **K** are summarized in Appendix A. They are then coded in the UEL to be used together with Abaqus Standard to achieve monolithic solution of THMC problems. The user-defined subroutines, the input files of the verification/validation tests presented in Section 4 and 5, and an instruction manual are available through the Supplementary Materials associated with this paper.

4. Verification tests

Considering the large size and the highly coupled nature of the system, the development and verification of the UEL shall follow a step-by-step strategy from the simple HM model to the THM model, and finally the comprehensive THMC model. Existing coupled HM and THM problems that

have closed-form solutions include: (1) Terzaghi's one-dimensional (1D) consolidation;[39] (2) Mandel's problem;[40] (3) thermoporoelastic bar subjected to temperature change on one end;[41] (4) cylindrical heat source in infinite porous medium.[42] Some of these solutions are based on assumptions and constitutive laws that differ from the ones adopted in this study. In order to verify our UEL which uses a specific thermoporoelastic model of Coussy[24] some of the aforementioned analytical solution must be revisited. In what follows, we will rederive the analytical solutions for problems #1 and #3 and refer to the solution of Cheng and Detournay[43] and McTigue[41] for problems #2 and #4, respectively. Finally, the THMC coupling will be examined through testing chemical species migration along a 1D thermoporoelastic bar.

4.1 Test #1 (HM): one-dimensional consolidation

Consider the classical 1D consolidation problem: a saturated porous layer with thickness H_{dr} for the one-way drainage condition subjected to constant vertical loading as shown in Fig. 3. Displacement and pore water flow is permitted only along the vertical direction. The celebrated solution by Terzaghi[39] assumes incompressible fluid and solid grain which is apparently no longer valid in Coussy's poroelasticity and thus requires a revisit. In the absence of thermal effect, fluid density evolution Equation (29) reduces to:

$$\dot{\rho}_f \qquad (49)$$

Substituting Equations (49) and (22) into the fluid mass balance Equation (4) and trimming all thermal related terms gives:

$$b\dot{\varepsilon}_{vol} + \left(\frac{1}{M} + \frac{n}{K^f}\right)\dot{p}_f \qquad \rho_f \nabla \cdot \mathbf{q}_f = 0 \qquad (50)$$

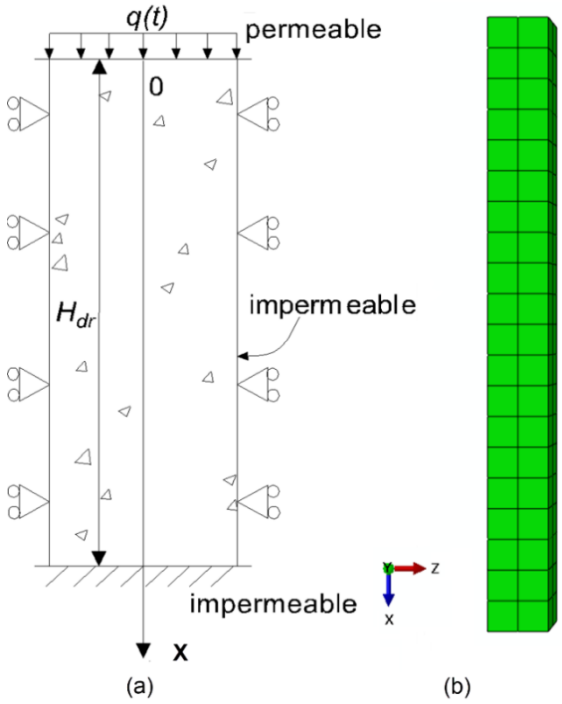

Fig. 3: Schematic diagram for 1D consolidation of a saturated porous column

Under 1D condition, volumetric strain equals to vertical strain ¿ ˙ ˙ according to Equation (21), where $M=K+4G/3$ is the constrained modulus of porous medium. Using this relation to eliminate ¿ ˙ and supply the Darcy's law Equation (25) into Equation (50), the PDE for 1D consolidation problem can be expressed as:

$$\frac{\partial P_f}{\partial t} = -\frac{b\mu}{Mk} C_v \frac{\partial \sigma_{xx}}{\partial t} + C_v \frac{\partial^2 P_f}{\partial x^2} \tag{51}$$

or

$$\frac{\partial P_f}{\partial t} = C_v \frac{\partial^2 P_f}{\partial x^2} \tag{52}$$

considering the case of constant total vertical load (i.e., $\partial\sigma_{xx}/\partial t=0$ for $t>0$). Here the pore fluid pressure $P_f(x,t)$ is the only unknown and C_v is the updated coefficient of consolidation:

$$C_v = \frac{k}{\mu\left(\frac{1}{N} + \frac{n}{K^f} + \frac{b^2}{M}\right)} \tag{53}$$

Equation (52) is formally identical to Terzaghi's consolidation equation and its solution can be readily achieved by using the updated coefficient of consolidation C_v in Terzaghi's solution. Numerical wise, a 10m-high porous column is modeled in Abaqus as shown in Fig. 3. The top boundary is set as drained and subjected to a constant surface pressure of 5 KPa. The bottom and the four lateral

boundaries are all constrained along its normal direction with an impermeable surface. The initial pore pressure for the entire porous column is zero and stress free. At t = 0, a vertical stress of 8 KPa is applied at the top boundary. Other parameters used are: E=10 MPa; v=0.3; k=1×10^{-15} m^2; μ=0.001 Pa·s; ρ_s =1.25×10^3 kg/m^3; ρ_f =1.0×10^3 kg/m^3; ϕ_0=0.2; K_f =2000 MPa; N=100 MPa; b=0.9.

The solution of Equation (52) and the FE results are plotted together in Fig. 4 in terms of dimensionless time factor T_v=$C_v t/H_{dr}^2$, dimensionless depth $\bar{X}$ =x/H_{dr}, and degree of consolidation U_x=[$P_{f,0}$-$P_f(x,t)$]/$P_{f,0}$, where $P_{f,0}$ is the initial pore pressure. The perfect agreement between the numerical and the analytical solutions verifies the coupled HM capability of the UEL in a 1D setting.

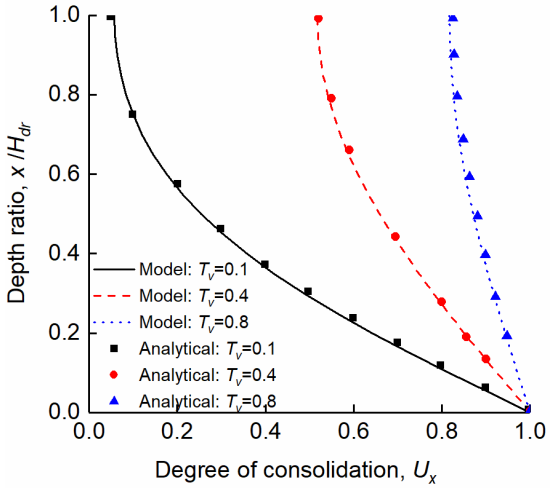

Fig. 4: 1D consolidation simulation results vs. analytical solution

4.2 Test #2 (HM): Mandel's problem

The second example aims to verify the HM coupling capability in 2D scenarios. We chose the Mandel's problem which consists of a $2a \times 2b$ porous rectangular sample sandwiched by two rigid, frictionless, and impermeable plates resulting a reaction force of $2F$ as shown in Fig. 5. The sample is fully drained and stress free along the horizontal direction. Solution of the Mandel's problem given by Coussy[24] is derived for constant-force condition. This means the top boundary is force-controlled and meanwhile can only have uniform vertical displacement. Numerically, only a quarter of the sample is simulated by the UEL to reduce computational cost as illustrated by Fig. 5. The following initial and boundary conditions are enforced on the quarter domain:

$$\begin{cases} \mathbf{u}(x,y,0)=0,\ P_f(x,y,0)=0; & 0<x<a, 0<y<b \\ u_x(0,y,t)=0,\ \mathbf{q}_f(0,y,t)=0; & t>0,\ 0<y<b \\ u_y(x,0,t)=0,\ \mathbf{q}_f(x,0,t)=0; & t>0, 0<x<a \\ \sigma_{xx}(a,y,t)=0, P_f(a,y,t)=0; & t>0,\ 0<y<b \\ \sigma_{yy}(x,b,t)=F/a,\ u_{xy}(x,b,t)=0, \mathbf{q}_f(x,b,t)=0; & t>0,\ 0<x<a \end{cases} \quad (54)$$

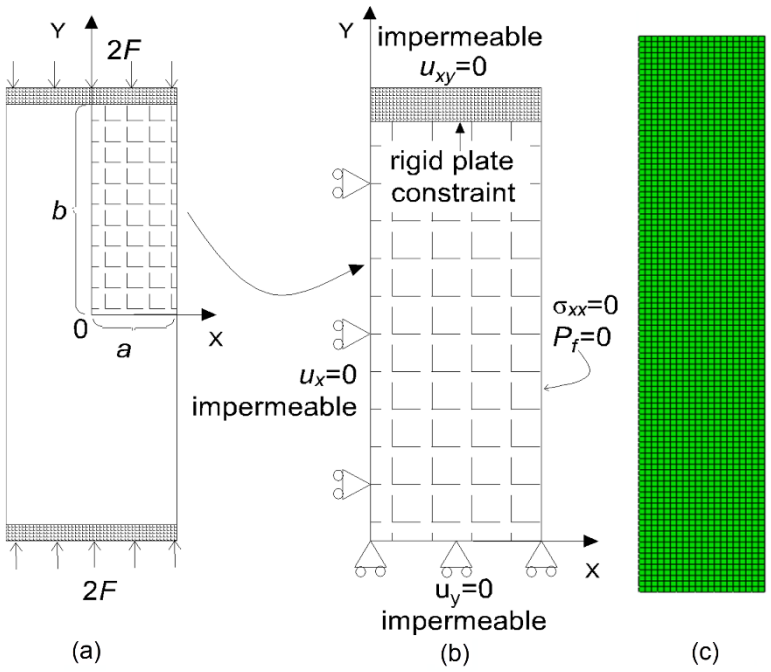

Fig. 5: Schematics of Mandel's problem[44] and the finite element model

The major challenge in numerical realization of this problem is the reproduction of the uniform vertical displacement on the top boundary in a force-controlled mode. The rigid upper plate cannot be easily represented, as the interaction between a rigid frictionless shell and a user-defined porous medium always induce numerical difficulties. The method adopted here is to approximate the top surface with a constant-pressure boundary, and at the same time using a sufficiently slender domain (low width-to-height ratio) to minimize the impact of unevenly distributed displacement at the top surface. It is found that when the width-to-height ratio reaches 0.2, the results become insensitive to further changes of the geometry. Fig. 6 plots the UEL results together with the analytical solution by Cheng and Detournay[43] Here the same poromechanical parameters as the previous verification test are used. Pressure is normalized by its initial value and the dimensionless time is defined as $\bar{t} = C_v t / a^2$ where C_v is defined in Equation (53). A satisfactory agreement is observed, confirming the HM capability of the UEL. It is worth noting that at early stage ($\bar{t} = 0.01, \bar{t} = 0.1$), the pore pressure at the central region rises above the initial value even when the lateral boundaries are drained. This signature feature of Mandel's problem is due to poroelastic effect at the system level, which is also successfully captured by the numerical model.

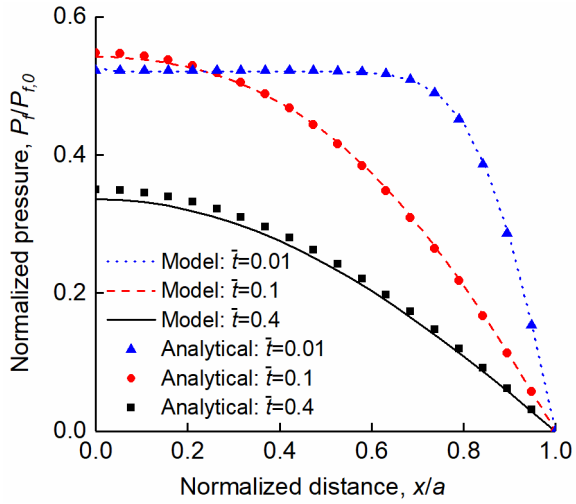

Fig. 6: Pressure distribution from Abaqus + UEL simulation and analytical solution[43]

4.3 Test #3 (THM): heating a 1D thermoporoelastic bar

Consider a semi-infinite thermoporoelastic bar, initially at a uniform temperature and pore pressure, subjected to a sudden temperature increase T^d at the boundary x=0. This boundary then remains drained and stress-free. The initial and boundary condition is defined as

$$\begin{cases} \sigma_{xx}(x,0) = P_f(x,0) = T(x,0) = 0; \quad x > 0 \\ u(0,t) = P_f(0,t) = 0, \; T(0,t) = T^d; \; t > 0 \end{cases} \tag{55}$$

McTigue[41] provided a solution for this problem but again with a different set of constitutive relations. A new closed-form solution consistent with the proposed governing equations therefore must be developed for verification purpose. Substituting the Darcy's law Equation (25) into the mass balance of fluid Equation (4) yields

$$\rho_f \dot{} \quad -3n\alpha_f \rho_f \dot{} \quad \nabla^2 P_f = 0 \tag{56}$$

Define $\alpha_m=\alpha_\phi+n\alpha_f$, consider porosity evolution from Equation (22), and substitute them into Equation (56):

$$b\dot{} \quad \dot{} \tag{57}$$

Simplifying the constitutive law Equation (21) for 1D case and considering the stress boundary condition, the volumetric strain increment can be expressed as:

$$d\varepsilon_v = d\varepsilon_{xx} = \frac{bdP_f + 3\alpha K dT}{M} \tag{58}$$

Substituting Equation (58) into Equation (57) gives:

$$\frac{1}{C_v}\frac{\partial P_f}{\partial t} + A\frac{\partial T}{\partial t} = \frac{\partial^2 P_f}{\partial x^2} \tag{59}$$

where

$$A = \frac{\mu}{k}\left(\frac{3\alpha bK}{M} - 3\alpha_m\right) \tag{60}$$

and C_v is the same as defined in Equation (53). Introducing normalized variables $\bar{P}_f = P_f / P_f^d$ and $\bar{T} = T / T^d$, where T^d is the prescribed temperature at x=0 and P_f^d is defined such that $C_v A T^d / P_f^d = 1$, Equation (59) now reduces to a standard wave equation:

$$\frac{\partial \bar{P}_f}{\partial t} + \frac{\partial \bar{T}}{\partial t} = C_v \frac{\partial^2 \bar{P}_f}{\partial x^2} \text{ and } P_f^d = C_v A T^d \tag{61}$$

On the other hand, the energy balance equation can be rewritten in terms of normalized variables by substituting Equations (27) and (58) into Equation (16) and considering 1D scenario:

$$B\frac{\partial \bar{P}_f}{\partial t} + \frac{\partial \bar{T}}{\partial t} + D\frac{\partial\left(c_f T \mathbf{q}_f\right)}{\partial x} = E\frac{\partial^2 \bar{T}}{\partial x^2} \tag{62}$$

where

$$B = \frac{\left[c_f \rho_f T\left(\frac{1}{N} + \frac{n}{K_f}\right) + \frac{\left(bc_f\rho_f - c_s\rho_s\right)Tb}{M}\right]P_f^d}{\left[c_b - 3\rho_f c_f \alpha_m T + \frac{3\left(bc_f\rho_f - c_s\rho_s\right)\alpha KT}{M}\right]T^d} \tag{63}$$

$$D = \frac{1}{\left[c_b - 3\rho_f c_f \alpha_m T + 3\left(bc_f\rho_f - c_s\rho_s\right)\alpha KT / M\right]T^d} \tag{64}$$

$$E = \frac{\kappa}{c_b - 3\rho_f c_f \alpha_m T + 3\left(bc_f\rho_f - c_s\rho_s\right)\alpha KT / M} \tag{65}$$

and $c_b = \left(1-n\right)\rho_s c_s + n\rho_f c_f$ is the bulk heat capacity per unit volume of porous media.

For typical values of parameters for geomaterials, the coefficients *B* and *D* are usually quite small and can be neglected,[24, 41] reducing Equation (62) into:

$$\frac{\partial \bar{T}}{\partial t} = E\nabla^2 \bar{T} \tag{66}$$

This conveniently decouples the heat equation Equation (16) from the H or M processes so that it can be solved separately. The analytical solution to Equation (66) associated with the initial boundary conditions Equation (55) is given by:

$$\bar{T} = 1 - erf\left(\frac{x}{2\sqrt{Et}}\right) \tag{67}$$

Substituting Equation (67) into Equation (61), the problem reduces to a standard parabolic PDE with respect to the normalized fluid pressure $\bar{P}_f$, the solution of which under condition (55) is given by:

$$\bar{P}_f = -\left(1-\frac{C_v}{E}\right)^{-1}\left[erf\left(\frac{x}{2\sqrt{C_v t}}\right)-erf\left(\frac{x}{2\sqrt{Et}}\right)\right] \tag{68}$$

The finite element model corresponding to this problem is shown in Fig. 7. To approximate the semi-infinite condition, the length-to-width ratio of model is made sufficiently large as 100. Lateral surfaces are impermeable, adiabatic, and can only move along the *x*-direction to ensure 1D condition. Initially, both P_f and T are zero everywhere. The left end is fixed, drained, and subjected to a constant temperature T^d=1 K. The right end is drained, constant temperature and stress free. All hydromechanical parameters are still the same with the verification test #1. The thermal parameters are specified as: c_s=800 J/(kg·K); c_f=4000 J/(kg·K); α=1.0×10^{-4} K^{-1}; α_f=3.0×10^{-4} K^{-1}; α_ϕ=0.4×10^{-4} K^{-1}.

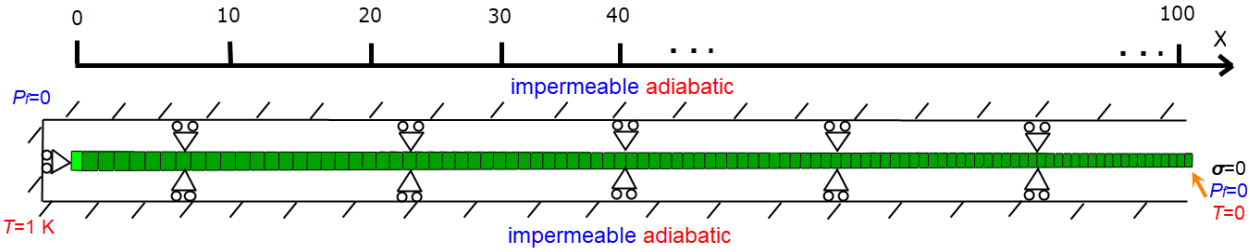

Fig. 7: Finite element model of a 1D thermoporoelastic bar

The numerical results and the analytical solutions are plotted in Fig. 8 and Fig. 9 in terms of normalized temperature $\bar{T}$, normalized pore pressure $\bar{P}_f$, and normalized *x*-coordinate $\bar{x} = x/\sqrt{C_v t}$ for different values of *R* which is defined as the ratio between the diffusion coefficient in Equation (53) and the thermal coefficient in Equation (65) (i.e., $R=C_v/E$). Thermal conductivity coefficient κ is determined as (κ = 91.3, 11.4, 5.7 W/(m·K)) corresponding to the selected *R* values (*R*=0.25, 2, 4) in respect. Perfect agreements between the FE model and the analytical solution are observed at a random time t=1.12×10^6 s regardless of the choice of *R* in this 1D THM coupling analysis.

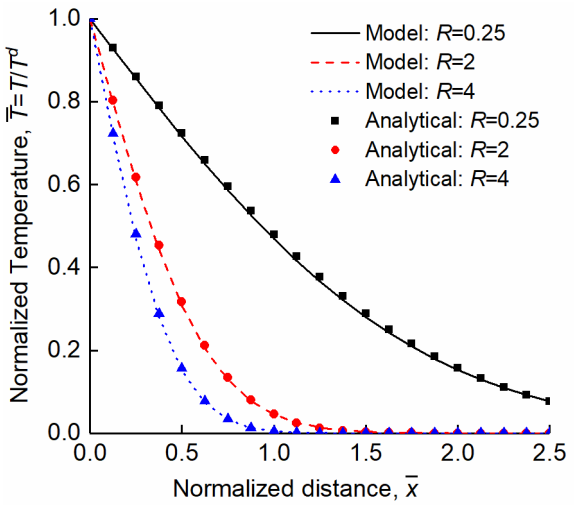

Fig. 8: Normalized temperature profile at t=1.12×10^6 s

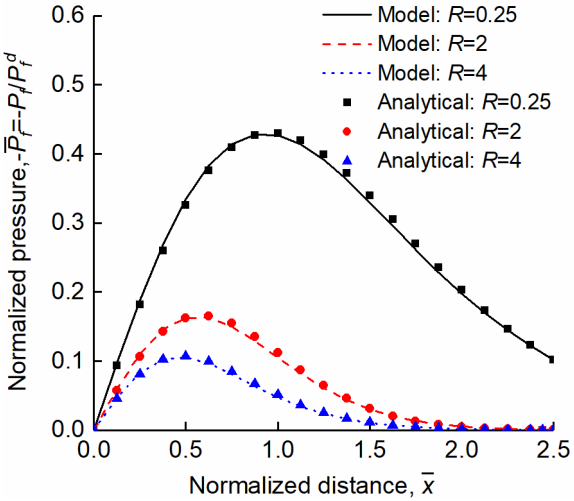

Fig. 9: Normalized pressure profile at t=1.12×10^6 s

4.4 Test #4 (THM): cylindrical heat source in an infinite space

For 3D THM verification, we investigate the problem of cylindrical heat source embedded in an infinite space. This geometry has been studied by Booker and Savvidou[42] to represent the problem of a canister of radioactive waste buried in saturated soil. The finite element mesh is shown in Fig. 10. A constant heat flux is applied on the heat source region marked in red. All five boundary surfaces are fixed in its normal direction. Fully drained and constant temperature boundary conditions are assigned to the exterior surface (i.e., ECD and ABED). Because the model represents a one-eighth of the full domain, the interior surfaces (i.e., OADC, OCEB, and OAB) in the current model are all undrained and adiabatic. Final parameters used in verification is the same with test #3 except for κ=1.14×10^{-2} W/(m·K). The power of the heat source is specified as 1 W/m^3.

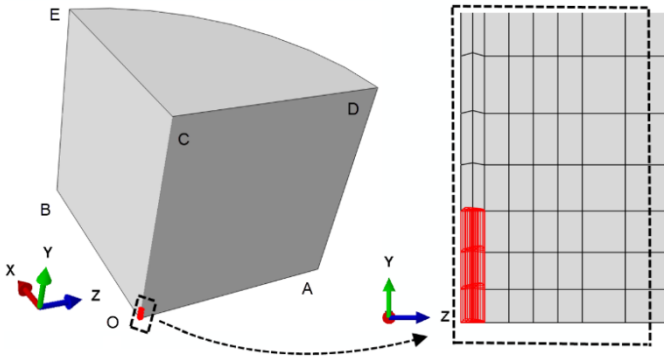

Fig. 10: Finite element model of an axisymmetric domain containing a cylindrical heat source

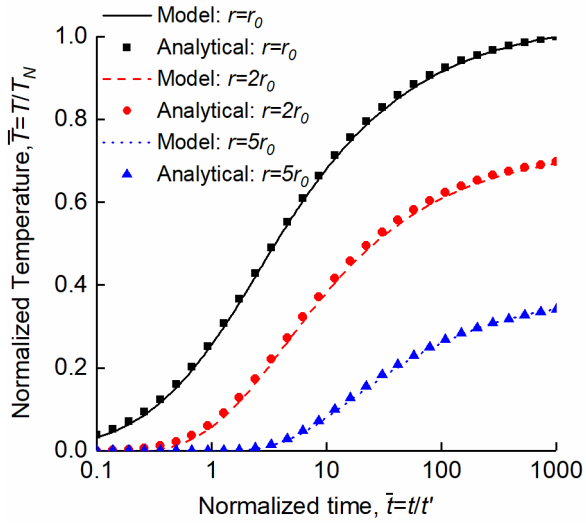

Fig. 11: Temperature evolution near a cylindrical heat source (analytical solution from Booker and Savvidou[42])

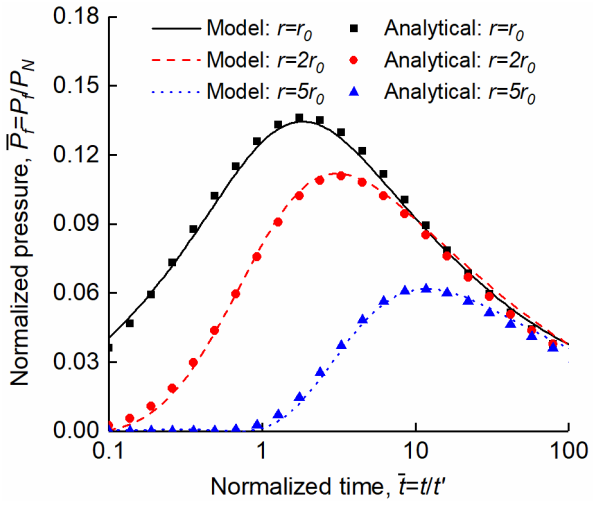

Fig. 12: Pore pressure evolution near a cylindrical heat source (analytical solution from Booker and Savvidou[42])

In Fig. 12 and Fig. 13, the temperature and pressure histories are compared with analytical solutions respectively, at three locations (r_0, $2r_0$, and $5r_0$) away from the heat source where r_0 is the radius of the canister. The temperature is normalized by a maximum value T_N at the midpoint on the surface of the heat source; pressure is normalized by P_N, which represents the maximum pressure if soil is impermeable (C_v=0). Time scale is also normalized by a factor $t' = r_0^2/\kappa$. The agreements for the temperature and pore pressure histories are excellent at all locations. This agreement, together with the previous three verification results, confirms that the THM governing equations are correctly solved by the UEL.

4.5 Test #5 (H-C): chemical species migration along a 1D thermoporoelastic bar

Verification of the UEL is not complete until the THM-C coupling is checked. Most past studies end their verification up to THM coupling, given the challenges involved in deriving closed-form solutions when chemical processes present. The current formulation assumes one-way coupling between THM and C, which entails a decoupled solution scheme where chemical molar concentration can be computed independently after the THM fields have been solved or prescribed. Considering the THM part has already been verified, the task here is to focus on verifying the HC coupling capability. Let us inspect chemical field equation first:

$$n\left(\frac{\partial C}{\partial t} - \frac{C}{\rho_f}\mathbf{q}_f\right) + \nabla\cdot(\mathbf{q}_C) = 0 \tag{69}$$

Since $\rho_f = \frac{P_f M}{RT}$ and $\mathbf{q}_C = -D_C \nabla C$, Equation (69) can be reorganized for 1D condition as:

$$C\left(\frac{b^2}{M} + \frac{1}{N}\right)\frac{\partial P_f}{\partial t} + \frac{\partial C}{\partial t} - \frac{\partial}{\partial x}\left(\frac{C}{\rho_f}\mathbf{q}_f\right) = D_C\frac{\partial^2 C}{\partial x^2} \tag{70}$$

Following the same normalization approach in Section 4.2.2 such that $P_f = P_f^d \bar{P}_f$, $T = T^d \bar{T}$ and $C = C^d \bar{C}$, a dimensionless expression for Equation (70) follows:

$$H\frac{\partial \bar{P}_f}{\partial t} + I\frac{\partial \bar{T}}{\partial t} + \frac{\partial \bar{C}}{\partial t} + \frac{\partial}{\partial x}\left(L\mathbf{q}_f\bar{C}\right) = R\frac{\partial^2 \bar{C}}{\partial x^2} \tag{71}$$

where

$$H = \left(\frac{b^2}{Mn} + \frac{1}{Nn}\right)\bar{C}P_f^d \tag{72}$$

$$I = 3\frac{Kb\alpha - M\alpha_\phi}{Mn}\bar{C}T^d \tag{73}$$

$$L = \frac{1}{n\rho_f} \tag{74}$$

$$R = \frac{D_C}{n} \tag{75}$$

For the case of steady-state $\bar{P}_f$ and $\bar{T}$ profiles (i.e., $\partial\bar{P}_f/\partial t = 0$ and $\partial\bar{T}/\partial t = 0$), Equation (71) reduces to an inhomogeneous convection-diffusion equation describing solute transport.

$$\frac{\partial\bar{C}}{\partial t} = R\frac{\partial^2\bar{C}}{\partial x^2} - L\mathbf{q}_f\frac{\partial\bar{C}}{\partial x} - \bar{C}\frac{\partial}{\partial x}\left(L\mathbf{q}_f\right) \tag{76}$$

Equation (76) is coupled with H through the advective term $L\mathbf{q}_f\bar{C}$ (or $v_f\bar{C}$ at 1D condition and v_s=0) originated from the motion of the solute-carrying fluid.[45] In predicting the transport of radio nuclide over a long time-span, the validity of solution will be impaired if the contribution of advection is neglected.[46] Great efforts have been made in the past decades to develop solution to convection-diffusion-reaction (CDR) equations from the condition of constant velocity[47] to spatially dependent velocity.[48, 49] Considering an initial and boundary condition as follows:

$$\begin{cases} C(x,0) = 0, \;\; P_f(x,0) = 0, T = 1\,K, & 0 < x < l \\ C(0,t) = C^d, \text{ mol/L}, v_f(0,t) = \pm 0.025 m/s; & t > 0 \\ C(l,t) = 0, \;\; v_f(l,t) = \mp \qquad\quad {}'s; & t > 0 \end{cases} \tag{77}$$

Zoppou and Knight[49] provides solution for this type of unsteady hyperbolic PDE in 1D finite domain, which will be used for comparison with numerical results given by the UEL.

$$\bar{C}(x,t) = \frac{1}{2}erfc\left(\frac{x - v_f t}{2\sqrt{Rt}}\right) + \frac{1}{2}\exp\left(\frac{v_f x}{R}\right)erfc\left(\frac{x + v_f t}{2\sqrt{Rt}}\right) \tag{78}$$

The simulation is built on the same geometry and mesh used for the verification test #3 (section 4.2.1). All hydromechanical parameters remain the same. The chemical diffusion coefficient D_c is set to 0.2 m^2/s. For the initial condition, we let P_f=0 MPa and C=0 mol/L everywhere in the domain. A constant contaminant molar concentration (0 mol/L→1 mol/L) and a constant fluid flux $\boldsymbol{q}_f$ is then enforced on the left and right end of domain for t>0. Since all lateral surfaces are impermeable, mass transfer is constrained in the x-direction. The resultant C profiles under different imposed flow rates at different times are plotted in Fig. 13. It is obvious that the chemicals transport faster when the bulk fluid flow direction is aligned, and the process is retarded when the bulk flow is against the

direction of concentration gradient drop. This implies that advection can greatly facilitate species migration near underground HLW repositories as the concentration and pressure gradients are always aligned. This coupling between H and C during mass transfer is expected and is encoded in the governing equations. Finally, the excellent match between the numerical and the analytical solutions presented in Fig. 13 certifies the successful realization of HC coupling by the UEL. Combining the THM and HC verification results, it is confirmed that the developed THMC UEL has correctly implemented the governing equations and can now be applied for full-scale case studies.

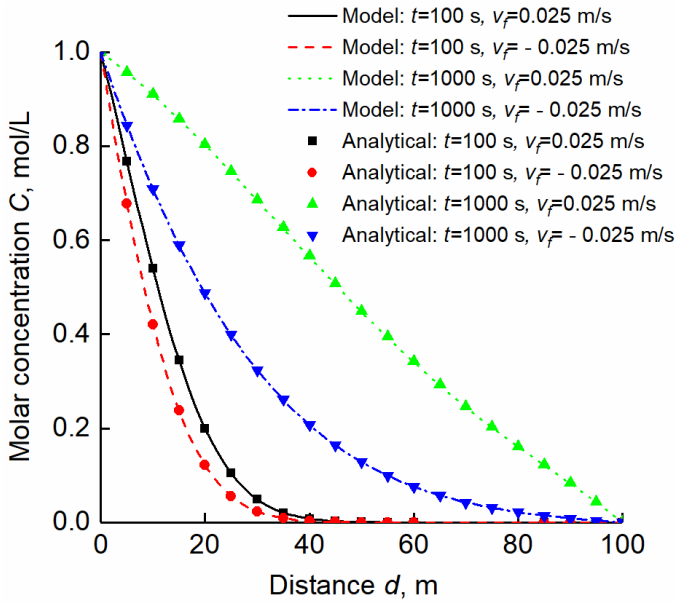

Fig. 13: Distribution of species molar concentration in a 1D porous bar (analytical solution from Zoppou and Knight[49])

5. Simulation of the ATLAS *in-situ* test

5.1 ATLAS experiment

Many in-situ tests have been conducted in the past decades to study the THM responses of host rocks due to heating generated by HLW canisters. One of them is the Admissible Thermal Loading for Argillaceous Storage (ATLAS) test conducted in the underground research facility HADES-URF (see Fig. 14) in Mol, Belgium at a depth of 223m.[50] The host formation, Boom clay, is an over-consolidated clay whose behavior can be roughly captured by thermo-elasticity in the small-strain regime.[10, 50] The ATLAS experiment consists of a horizontal main borehole (length=19 m, diameter=0.19 m) drilled from the test drift (diameter=3.5-4.7 m), with electrical heaters installed in the last 8 m of borehole.[51] According to François et al.[50], the first heating phase happened in July 1993 with the power of 900 W. About 3 years later, the second heating phase started by a sudden

increase of the power to 1800 W. The test is then terminated one year later followed by a natural cooling phase. Fig. 15 presents the history of heat flux from heaters on the main borehole.

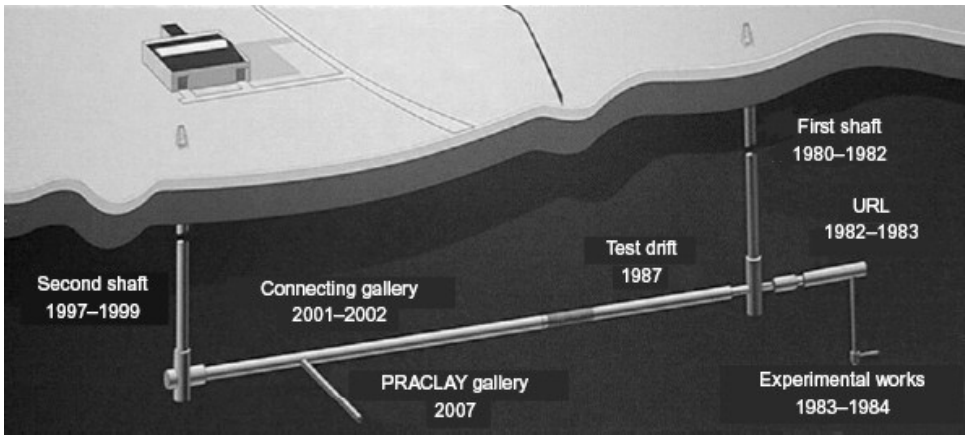

Fig. 14: Schematic view of the HADES Underground Research Facility in Mol, Belgium [25]

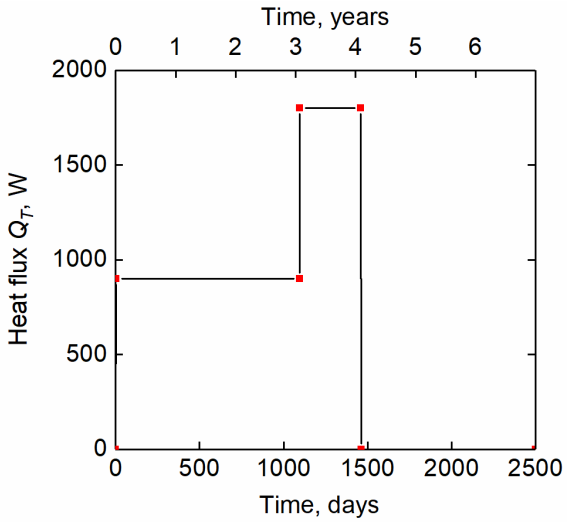

Fig. 15: Thermal loading history of the heater

5.2 Numerical simulation setup

Fig. 16a sketches the dimensions of the ATLAS test. The main borehole was accompanied by two parallel boreholes with instrumentation installed at 15 m away from the test drift. One of the observation boreholes (AT85E), was drilled 1.515 m away from the main borehole in the same horizontal plane, which is used to record changes in temperature, pore water pressure and total stress.[52] For numerical analysis here, the domain of interest is bounded by a 3D axisymmetric cylindrical surface (diameter=height=200 m) with the heater located at the center (Fig. 16b). At such a large scale, the disturbance of the THM field by the test drift which only occupies a small volume (3.5~4.7 m in diameter) can be neglected. Therefore, the problem is approximately axisymmetric, and only one-eighth of the domain is simulated in the FE model (Fig. 16c).

Although the ATLAS test was designed to monitor the coupled THM processes in the host formation, our simulation will also examine the spread of containment species following a hypothetical leakage event at t=0. Given the lack of leakage events documented in the literature for a realistic case study, the purpose of simulating a hypothetical leakage is merely to show the capability of the UEL in handling a full THMC boundary value problem. The boundary conditions for displacement (M), thermal flux (T), water flux (H), and species concentration (C) are applied at the heater-rock interface marked with red color in Fig. 16c. Note that the heater itself is not directly simulated in the FE model. To replicate the full loading history in ATLAS, the imposed thermal flux Q_T is made consistent with the thermal loading history presented in Fig. 15. The hypothetical leakage event is simulated by imposing a constant molar concentration (C=2 mmol/L) of the contaminate species at the heater's surface. The outer boundary of the domain ABDE and BCE (highlighted by blue wavy lines in Fig. 16c) are water/chemical permeable, heat conducting, and pressurized by in-situ geostatic stresses (i.e., P_f= 2.025 MPa, C=0.01 mol/L, T=16.5˚C, σ_v=σ_h=4.5 MPa). The symmetric boundaries OABC, ODEC and OAD are fixed in normal direction with no water, chemical and thermal fluxes allowed.

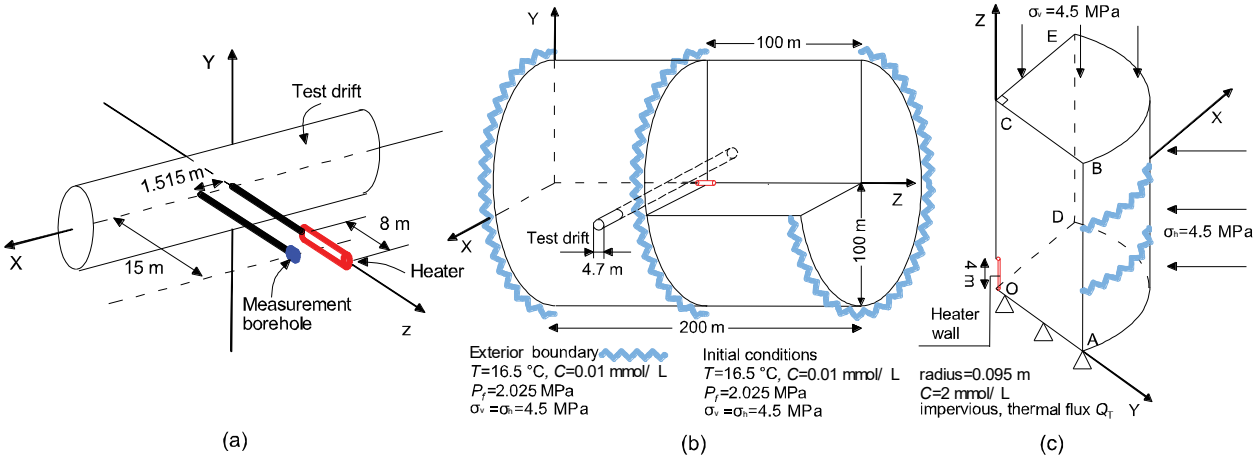

Fig. 16: a) schematic of the ATLAS experiment; b) idealization of the problem with boundary and initial conditions; c) the finite element model

The THMC parameters used for numerical modeling are presented in

Table 2. The THM parameters are selected according to the reported properties for Boom clay in ATLAS experiments[10, 51] and the typical values of thermoporoelastic properties for geomaterials summarized in Coussy[24] The chemical diffusivity is estimated based on the effective diffusion coefficients for dissolved species in Boom Clay measured by Jacops et al.[53]. In the Abaqus, the FE mesh is assigned with the developed THMC UEL. An element located 1.42 m away from the heater surface will play the role of measurement borehole in the model. The values of field variables extracted from this element will be used for benchmarking and inferring contaminant condition along with all near field nodes.

5.3 Results and discussion

The comparison between the results obtained from the current study and ATLAS experiment are presented in Fig. 17-19. Fig. 17 shows the temperature variation history at measurement point in 2500 days caused by the prescribed heating history described in Fig. 15. The simulated results are in good agreement with experiment data, indicating that heat transfer occurring at the near field is well captured by current model. Fig. 18 compares the predicted thermal-induced pore pressure variation with the field data. It is observed that, during the first heating phase, pressure surge rapidly at the beginning and then smoothly dropped even the power of the heater is kept same. Similar response occurs in the second heating phase except with a slightly steeper tendency in decline. The pore pressure rapidly reduces after the heater is turned off, and then gradually dissipates in the remaining time. Overall, the predicted pressure history matches well with the measured data in terms of the aforementioned pressure change characteristics. The slight discrepancy between the predicted and the measured minimum pore pressure (around t = 1500 days) may be remediated by incorporating more physics in the governing equations (e.g., temperature dependency of the dynamic viscosity). Our parametric study (not shown here) also suggests that thermal-induced pressurization is positively correlated with thermal expansion coefficient (α_f), while inversely dependent on the fluid flux rate ($\boldsymbol{q}_f$), and the compressibility of the pore fluid ($1/K_f$) and the porous material ($1/G$ and $1/K$).

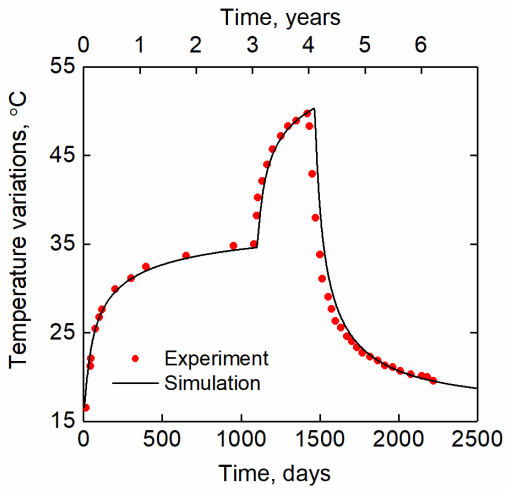

Fig. 17: Temperature evolution at the measurement borehole (experiment data from François et al.[50])

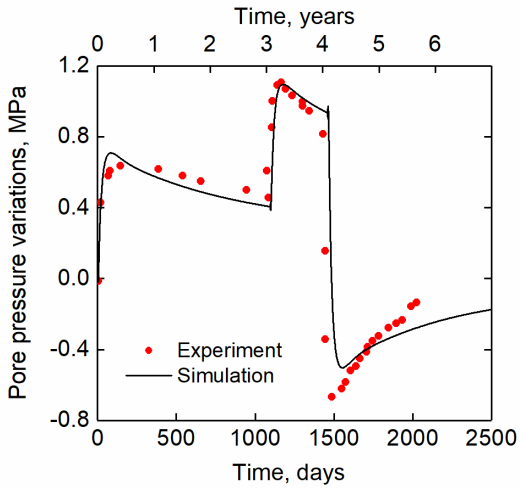

Fig. 18: Pore pressure evolution at the measurement borehole (experiment data from François et al.[50])

Fig. 19 presents the predicted and the measured variations of total circumferential stress with time. The agreement is satisfactory during the first heating phase. However, the simulated results start to deviate from the field data near the end of the second heating and the cooling phases. A closer observation shows that the predicted stress increases or maintains relatively constant during heating and monotonically decreases in cooling, while the field data suggests some degree of stress relaxation in heating and stress restoration in cooling. Similar discrepancy has been reported in other numerical simulation of the ATLAS test,[54] but no consensus has arrived regarding its causes yet.[50] Bernier and Neerdael[55] suggested that such deviation might be due to thermal interferences on the measurement devices. We suspect that some viscoelastic or viscoplastic deformations[56] have occurred in the Boom clay formation, which caused the relaxation of the thermal-induced stresses surrounding the heater. Furthermore, the host rock (Boom Clay) may develop some degree of

desaturation under the effect of heating, which may have also contributed to the discrepancy between the model prediction and the field data.

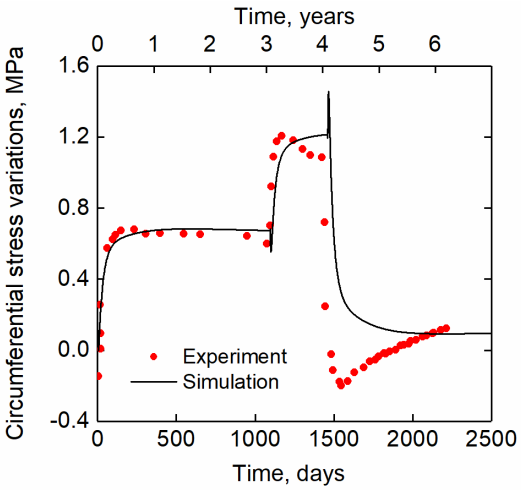

Fig. 19: Circumferential stress variation at the measurement borehole (experiment data from François et al.[50])

Fig. 20 shows the time history of contaminant concentration at three locations, following an assumed leakage event at *t*=0. It is apparent that the concentration increases faster close to the canister. Such growth slows down at larger times but still maintains an increasing tendency even at *t*=2500 days. Note that oscillations for several curves near t=1000 days and 1500 days are caused by the abrupt change of the heater power at the beginning and the end of the second phase. These sudden changes of the boundary condition are also responsible for the similar oscillations observed in the fluid pressure and the stress histories shown in Figs. 18 and 19, respectively. This is a common byproduct of using conventional Galerkin method on transient advection-diffusion problems. Although they disappear in later time steps and are not likely to impair overall results in current case study, the oscillations can be circumvented by adopting advanced finite element methods, such as the Subgrid Scale/Gradient Subgrid Scale (SGS/GSGS) method,[46] Streamline Upwind Petrov-Galerkin (SUPG)[57, 58] or Finite Increment Calculus (FIC) procedure.[59]

Fig. 21 shows the C distribution along the radius at different times. The model predicts that the contaminant is unlikely to reach 3 m away from the canister after 2500 days, even though the species migration has been accelerated by the advective bulk fluid flow since the beginning of heating. This demonstrates the excellent sealing properties of Boom clay in retarding the leakage of contaminants following a critical event.

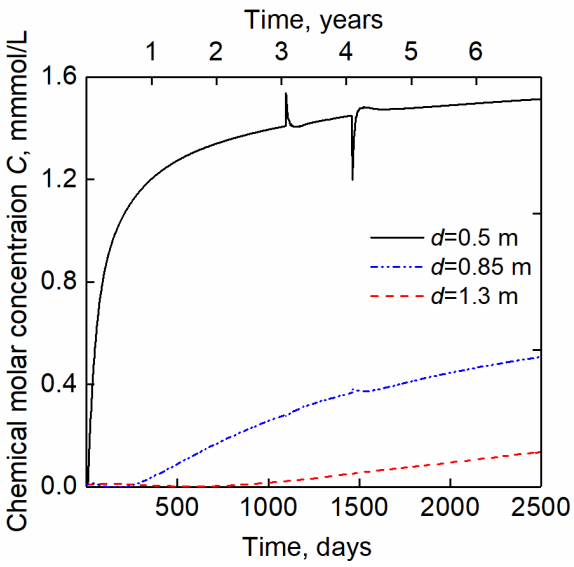

Fig. 20: Molar concentration evolution near the leakage source

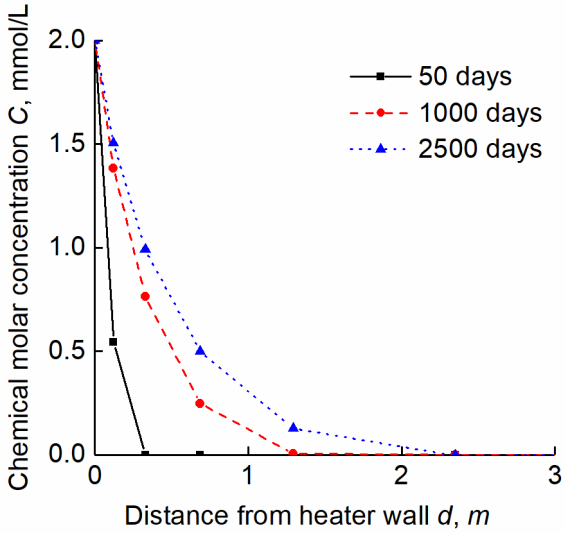

Fig. 21: Distribution of molar concentration along the radius of the domain

6. Concluding remarks

In this paper, a THMC UEL with a thermoporoelastic constitutive model is successfully implemented. A comprehensive set of verification tests have been conducted to check the correctness of the implementation at each coupling level. In this process, several analytical solutions are revisited and rederived to be consistent with the specific governing and constitutive equations adopted in this study. The verified UEL is then applied to simulate a full-scale heater test, and the modeling results exhibit good agreement with the field measurements. The ability to simulate diffusion and advection of chemical species coupled with THM loading makes the developed UEL a versatile and efficient tool in addressing geological HLW disposal problems.

The full implementation details including the derivation of governing equations, discretization, residuals, and Jacobian terms are presented. The UEL codes, the input files associated with each verification test and the ATLAS case study, and a user instruction are provided via Supplementary Materials. We hope the details of the numerical procedure presented here can facilitate the numerical realization of other THMC or general multiphysical solvers. Specifically, expansions can be made regarding the physical processes at concern by upgrading the field equations, material models, and element types. The Material module unlocks the potential of the code to integrate with advanced constitutive models for more precise modeling of different rock formations. In this regard, the authors is currently implementing a time-dependent microcrack damage model[60] in Material to couple with the proposed THMC UEL with the goal to evaluate the long-term microstructural evolution of host rocks subjected to sustained heating. Another possible extension at the Material level is to incorporate possible coupling between various diffusion mechanisms in the conduction laws (i.e., the generalized Darcy's and Fick's laws[61]). This is important for capturing in coupled mass transport phenomena such as osmotic flow,[62] buoyancy effect,[63] and Soret effect[64] in porous geological materials.

Acknowledgement

This research was supported by the U.S. National Science Foundation (NSF) under NSF CMMI Award No. 2113474 and the U.S. Department of Energy through grant DE-NE0008771 .

References

1. Rosner, R. and R. Lordan, *Why America should move toward dry cask consolidated interim storage of used nuclear fuel.* Bulletin of the Atomic Scientists, 2014. **70**(6): p. 48-62.
2. Ouzounian, G., S. Voinis, and F. Boissier, *Radioactive waste management in France: safety demonstration fundamentals.* Annals of the ICRP, 2012. **41**(3-4): p. 286-293.
3. Yeh, G.-T. and C.-H. Tsai, *Coupled THMC processes in radionuclide waste management.* 2017.
4. Rutqvist, J., et al., *Thermohydromechanics of partially saturated geological media: governing equations and formulation of four finite element models.* International journal of rock mechanics and mining sciences, 2001. **38**(1): p. 105-127.
5. Kolditz, O., et al., *OpenGeoSys: an open-source initiative for numerical simulation of thermo-hydro-mechanical/chemical (THM/C) processes in porous media.* Environmental Earth Sciences, 2012. **67**(2): p. 589-599.
6. Kolditz, O., et al., *Thermo-Hydro-Mechanical Chemical Processes in Fractured Porous Media: Modelling and Benchmarking*. Vol. 25. 2016: Springer.
7. Nagel, T., et al., *Computational Geotechnics: Storage of Energy Carriers*. 2017: Springer.
8. UT-Battelle, L., *HYDROGEOCHEM 5.0: A Three-Dimensional Model of Coupled Fluid Flow, Thermal Transport, and HYDROGEOCHEMical Transport through Variably Saturated Conditions: Version 5.0.* 2004.

9. Damiani, L.H., et al., *A framework for reactive transport modeling using FEniCS–Reaktoro: governing equations and benchmarking results.* Computational Geosciences, 2020: p. 1-15.
10. Tamizdoust, M.M. and O. Ghasemi-Fare, *A fully coupled thermo-poro-mechanical finite element analysis to predict the thermal pressurization and thermally induced pore fluid flow in soil media.* Computers and Geotechnics, 2020. **117**: p. 103250.
11. Sun, X., H. Luo, and K. Soga, *A coupled thermal–hydraulic–mechanical–chemical (THMC) model for methane hydrate bearing sediments using COMSOL Multiphysics.* Journal of Zhejiang University-SCIENCE A, 2018. **19**(8): p. 600-623.
12. Tao, J., et al., *Coupled thermo-hydro-mechanical-chemical modeling of permeability evolution in a CO2-circulated geothermal reservoir.* Geofluids, 2019. **2019**.
13. Kelkar, S., et al., *A simulator for modeling coupled thermo-hydro-mechanical processes in subsurface geological media.* International Journal of Rock Mechanics and Mining Sciences, 2014. **70**: p. 569-580.
14. Feng, X.-T., P.-Z. Pan, and H. Zhou, *Simulation of the rock microfracturing process under uniaxial compression using an elasto-plastic cellular automaton.* International Journal of Rock Mechanics and Mining Sciences, 2006. **43**(7): p. 1091-1108.
15. Pan, P.-Z., et al., *An approach for simulating the THMC process in single novaculite fracture using EPCA.* Environmental Earth Sciences, 2016. **75**(15): p. 1-16.
16. Rutqvist, J., *Status of the TOUGH-FLAC simulator and recent applications related to coupled fluid flow and crustal deformations.* Computers & Geosciences, 2011. **37**(6): p. 739-750.
17. Taron, J., D. Elsworth, and K.-B. Min, *Numerical simulation of thermal-hydrologic-mechanical-chemical processes in deformable, fractured porous media.* International Journal of Rock Mechanics and Mining Sciences, 2009. **46**(5): p. 842-854.
18. Xu, T., et al., *TOUGHREACT user's guide: A simulation program for non-isothermal multiphase reactive geochemical transport in variable saturated geologic media*. 2004, Lawrence Berkeley National Lab.(LBNL), Berkeley, CA (United States).
19. Zheng, L., et al., *Coupled THMC models for bentonite in an argillite repository for nuclear waste: Illitization and its effect on swelling stress under high temperature.* Engineering geology, 2017. **230**: p. 118-129.
20. Thararoop, P., Z.T. Karpyn, and T. Ertekin, *Development of a multi-mechanistic, dual-porosity, dual-permeability, numerical flow model for coalbed methane reservoirs.* Journal of Natural Gas Science and Engineering, 2012. **8**: p. 121-131.
21. Kim, J., E. Sonnenthal, and J. Rutqvist, *A sequential implicit algorithm of chemo-thermo-poro-mechanics for fractured geothermal reservoirs.* Computers & Geosciences, 2015. **76**: p. 59-71.
22. Poulet, T. and M. Veveakis, *A viscoplastic approach for pore collapse in saturated soft rocks using redback: an open-source parallel simulator for rock mechanics with dissipative feedbacks.* Computers and Geotechnics, 2016. **74**: p. 211-221.
23. Sun, W., *A stabilized finite element formulation for monolithic thermo - hydro - mechanical simulations at finite strain.* International Journal for Numerical Methods in Engineering, 2015. **103**(11): p. 798-839.
24. Coussy, O., *Poromechanics*. 2004, Chichester: John Wiley & Sons, Ltd.
25. Bastiaens, W. and F. Bernier. *25 years of underground engineering in a plastic clay formation: the HADES underground research laboratory*. in *Geotechnical aspects of underground construction in soft ground. Proceedings of the 5th international conference of TC 28 of the ISSMGE, the Netherlands, 15-17 june 2005*. 2006.
26. Manepally, C., et al., *Coupled Processes Workshop Report*. 2011, Technical Report. Center for Nuclear Waste Regulatory Analyses and the US ….
27. Zhang, Y., *Mechanics of adsorption–deformation coupling in porous media.* Journal of the Mechanics and Physics of Solids, 2018. **114**: p. 31-54.

28. Zhou, X., S. Liu, and Y. Zhang, *Permeability Evolution of Fractured Sorptive Geomaterials: A Theoretical Study on Coalbed Methane Reservoir.* Rock Mechanics and Rock Engineering, 2021. **54**: p. 3507–3525
29. Ciantia, M.O., R. Castellanza, and C. Di Prisco, *Experimental study on the water-induced weakening of calcarenites.* Rock Mechanics and Rock Engineering, 2015. **48**: p. 441-461.
30. Zhang, X. and C. Spiers, *Compaction of granular calcite by pressure solution at room temperature and effects of pore fluid chemistry.* International Journal of Rock Mechanics and Mining Sciences, 2005. **42**(7-8): p. 950-960.
31. Chester, S.A., C.V. Di Leo, and L. Anand, *A finite element implementation of a coupled diffusion-deformation theory for elastomeric gels.* International Journal of Solids and Structures, 2015. **52**: p. 1-18.
32. Bouklas, N., et al., *A nonlinear, transient finite element method for coupled solvent diffusion and large deformation of hydrogels.* 2015. **79**: p. 21-43.
33. Murad, M.A. and A.F.J.I.J.f.N.M.i.E. Loula, *On stability and convergence of finite element approximations of Biot's consolidation problem.* 1994. **37**(4): p. 645-667.
34. White, J.A. and R.I. Borja, *Stabilized low-order finite elements for coupled solid-deformation/fluid-diffusion and their application to fault zone transients.* Computer Methods in Applied Mechanics and Engineering, 2008. **197**(49-50): p. 4353-4366.
35. Choo, J. and R.I. Borja, *Stabilized mixed finite elements for deformable porous media with double porosity.* Computer Methods in Applied Mechanics and Engineering, 2015. **293**: p. 131-154.
36. Park, K. and G.H. Paulino, *Computational implementation of the PPR potential-based cohesive model in ABAQUS: Educational perspective.* Engineering fracture mechanics, 2012. **93**: p. 239-262.
37. Msekh, M.A., et al., *Abaqus implementation of phase-field model for brittle fracture.* Computational Materials Science, 2015. **96**: p. 472-484.
38. Balzani, D., et al., *Numerical calculation of thermo-mechanical problems at large strains based on complex step derivative approximation of tangent stiffness matrices.* Computational Mechanics, 2015. **55**(5): p. 861-871.
39. Terzaghi, K., *Theoretical soil mechanics, Wiley, New York.* 1943.
40. Mandel, J., *Consolidation des sols (étude mathématique).* Geotechnique, 1953. **3**(7): p. 287-299.
41. McTigue, D., *Thermoelastic response of fluid - saturated porous rock.* Journal of Geophysical Research: Solid Earth, 1986. **91**(B9): p. 9533-9542.
42. Booker, J.R. and C. Savvidou, *Consolidation around a point heat source.* International Journal for Numerical and Analytical Methods in Geomechanics, 1985. **9**(2): p. 173-184.
43. Cheng, A.H.D. and E. Detournay, *A direct boundary element method for plane strain poroelasticity.* International Journal for Numerical and Analytical Methods in Geomechanics, 1988. **12**(5): p. 551-572.
44. Phillips, P.J., *Finite element methods in linear poroelasticity: Theoretical and computational results*. 2005.
45. Kim, A.S., *Complete analytic solutions for convection-diffusion-reaction-source equations without using an inverse Laplace transform.* Scientific reports, 2020. **10**(1): p. 1-13.
46. Yin, S., et al., *Fully coupled THMC modeling of wellbore stability with thermal and solute convection considered.* Transport in porous media, 2010. **84**(3): p. 773-798.
47. Ogata, A. and R.B. Banks, *A solution of the differential equation of longitudinal dispersion in porous media: fluid movement in earth materials*. 1961: US Government Printing Office.
48. Kumar, A., D.K. Jaiswal, and N. Kumar, *Analytical solutions to one-dimensional advection–diffusion equation with variable coefficients in semi-infinite media.* Journal of Hydrology, 2010. **380**(3-4): p. 330-337.

49. Zoppou, C. and J. Knight, *Analytical solutions for advection and advection-diffusion equations with spatially variable coefficients.* Journal of Hydraulic Engineering, 1997. **123**(2): p. 144-148.
50. François, B., L. Laloui, and C. Laurent, *Thermo-hydro-mechanical simulation of ATLAS in situ large scale test in Boom Clay.* Computers and Geotechnics, 2009. **36**(4): p. 626-640.
51. Chen, G., et al., *ATLAS III in situ heating test in boom clay: Field data, observation and interpretation.* Computers and Geotechnics, 2011. **38**(5): p. 683-696.
52. De Bruyn, D. and S. Labat, *The second phase of ATLAS: the continuation of a running THM test in the HADES underground research facility at Mol.* Engineering Geology, 2002. **64**(2-3): p. 309-316.
53. Jacops, E., et al., *The dependency of diffusion coefficients and geometric factor on the size of the diffusing molecule: observations for different clay-based materials.* Geofluids, 2017. **2017**.
54. Jeffries, R., *Interclay II project- a coordinated benchmark exercise on the rheology of clays(Report on stages 2 and 3).* EUR(Luxembourg), 1995.
55. Bernier, F. and B. Neerdael, *Overview of in-situ thermomechanical experiments in clay: Concept, results and interpretation.* Engineering geology, 1996. **41**(1-4): p. 51-64.
56. Yu, H.D., et al., *Creep behavior of boom clay.* International Journal of Rock Mechanics and Mining Sciences, 2015: p. 256-264.
57. Brooks, A.N. and T.J. Hughes, *Streamline upwind/Petrov-Galerkin formulations for convection dominated flows with particular emphasis on the incompressible Navier-Stokes equations.* Computer methods in applied mechanics and engineering, 1982. **32**(1-3): p. 199-259.
58. Christie, I., et al., *Finite element methods for second order differential equations with significant first derivatives.* International Journal for Numerical Methods in Engineering, 1976. **10**(6): p. 1389-1396.
59. Oñate, E., *Derivation of stabilized equations for numerical solution of advective-diffusive transport and fluid flow problems.* Computer methods in applied mechanics and engineering, 1998. **151**(1-2): p. 233-265.
60. Sisodiya, M., Zhang, Y., *A rate-dependent directional damage theory for brittle rocks considering the kinetics of microcrack growth.* Rock Mechanics and Rock Engineering, 2021: p. accepted.
61. Hassanizadeh, S.M., *Derivation of basic equations of mass transport in porous media, Part 2. Generalized Darcy's and Fick's laws.* Advances in Water Resources, 1986. **9**(4): p. 207-222.
62. Huyghe, J.M. and J.D. Janssen, *Quadriphasic mechanics of swelling incompressible porous media.* International Journal of Engineering Science, 1997. **35**(8): p. 793-802.
63. Trevisan, O.V. and A. Bejan, *Natural convection with combined heat and mass transfer buoyancy effects in a porous medium.* International Journal of Heat and Mass Transfer, 1985. **28**(8): p. 1597-1611.
64. Jamet, P., et al., *The thermogravitational effect in porous media: a modelling approach.* Transport in porous media, 1992. **9**(3): p. 223-240.

Appendix A: Implementation details of the THMC UEL

Three dimensional isoparametric element

Over an element Ω^e, we define the coordinate mapping using nodal shape functions as follows:

$$\mathbf{x}(\boldsymbol{\xi}) = \mathbf{N}(\boldsymbol{\xi})\,\mathbf{x} \tag{A1}$$

where ***N*** is the shape function matrix, $\boldsymbol{\xi}=(\xi, \eta, \zeta)$ constitute a reference coordinate system shown in Fig. A.

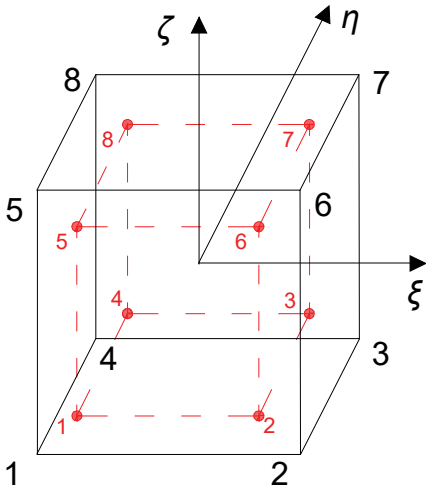

Fig. A: Three dimensional trilinear hexahedral isoparametric reference element

For the three-dimensional 8 node trilinear hexahedral element, the node ordering in the natural coordinates is shown in Fig. A. Accordingly, the shape functions for this type of element with respect to the reference coordinates are given by:

$$\begin{cases} N_1 = \frac{1}{8}(1-\xi)(1-\eta)(1-\zeta),\ N_2 = \frac{1}{8}(1+\xi)(1-\eta)(1-\zeta), \\ N_3 = \frac{1}{8}(1+\xi)(1+\eta)(1-\zeta),\ N_4 = \frac{1}{8}(1-\xi)(1+\eta)(1-\zeta), \\ N_5 = \frac{1}{8}(1-\xi)(1-\eta)(1+\zeta),\ N_6 = \frac{1}{8}(1+\xi)(1-\eta)(1+\zeta), \\ N_7 = \frac{1}{8}(1+\xi)(1+\eta)(1+\zeta),\ N_8 = \frac{1}{8}(1-\xi)(1+\eta)(1+\zeta) \end{cases} \tag{A2}$$

The infinitesimal strain **ε** can be subsequently defined as:

$$\boldsymbol{\varepsilon} = \begin{bmatrix} \varepsilon_{11} \\ \varepsilon_{22} \\ \varepsilon_{33} \\ \varepsilon_{23} \\ \varepsilon_{13} \\ \varepsilon_{12} \end{bmatrix} = \begin{bmatrix} \frac{\partial}{\partial x} & 0 & 0 \\ 0 & \frac{\partial}{\partial y} & 0 \\ 0 & 0 & \frac{\partial}{\partial z} \\ 0 & \frac{\partial}{\partial z} & \frac{\partial}{\partial y} \\ \frac{\partial}{\partial z} & 0 & \frac{\partial}{\partial x} \\ \frac{\partial}{\partial y} & \frac{\partial}{\partial x} & 0 \end{bmatrix} \begin{bmatrix} u_1 \\ u_2 \\ u_3 \end{bmatrix} = \nabla_s \mathbf{N} \quad \text{(A3)}$$

This can be further simplified by relating with Equation (43) as $\boldsymbol{\varepsilon} = \mathbf{B}$.

Jacobian

In addition to residuals, the Jacobian terms in Equation (44) are also required by the iterative solver which uses the Newton-Rapson scheme. For conciseness, all kinematics and state variables are referred at the next time step with the notation (*t*+Δ*t*) omitted.

Jacobian of M equation

First, recalling Equation (45), the Jacobian for the M equation can be derived as:

$$\mathbf{K}_{uu} = -\frac{\partial \mathbf{R}}{\partial \mathbf{u}} \qquad \text{(A4)}$$

Considering $\mathbf{u} = \mathbf{N}$, we have , then $= \mathbf{D}_{mm}\mathbf{B}$. Further noticing and $\mathbf{D}_{nm} = \begin{bmatrix} b-n & b-n & b-n & 0 & 0 & 0 \end{bmatrix}$, Equation (A4) can be rewritten as:

$$\mathbf{K}_{uu} = \int_{\Omega} \mathbf{B}^T \mathbf{D}_{mm} \mathbf{B} d\Omega + \left(\rho_s - \rho_f\right) \mathbf{g} \int_{\Omega} \mathbf{D}_{nm} \mathbf{B} d\Omega \quad \text{(A5)}$$

where

$$\mathbf{D}_{mm}=\frac{\partial\boldsymbol{\sigma}}{\partial\boldsymbol{\varepsilon}}=\begin{bmatrix} K+\frac{4}{3}G & K-\frac{2}{3}G & K-\frac{2}{3}G & 0 & 0 & 0\\ K-\frac{2}{3}G & K+\frac{4}{3}G & K-\frac{2}{3}G & 0 & 0 & 0\\ K-\frac{2}{3}G & K-\frac{2}{3}G & K+\frac{4}{3}G & 0 & 0 & 0\\ 0 & 0 & 0 & 2G & 0 & 0\\ 0 & 0 & 0 & 0 & 2G & 0\\ 0 & 0 & 0 & 0 & 0 & 2G \end{bmatrix}$$

Similarly, for the HM coupling term, we have

$$\begin{aligned}\mathbf{K}_{uP}&=-\frac{\partial\int_\Omega\mathbf{B}^T\boldsymbol{\sigma}d\Omega}{\partial\mathbf{u}_f}-\frac{\partial\int_\Omega\mathbf{N}^T\mathbf{b}d\Omega}{\partial\mathbf{u}_f}\\ &=\int_\Omega\mathbf{B}^T\frac{\partial\boldsymbol{\sigma}}{\partial P_f}\frac{\partial P}{\partial\mathbf{u}_f}\\ &=\int_\Omega\mathbf{B}^T\mathbf{D}_{mh}\mathbf{N}d\Omega+\left(\rho_s-\rho_f\right)\int_\Omega\mathbf{N}^T\mathbf{g}\mathbf{D}_{nh}\mathbf{N}d\Omega\end{aligned}\tag{A6}$$

where $\mathbf{D}_{mh}=\begin{bmatrix}-b & -b & -b & 0 & 0 & 0\end{bmatrix}^T$ and $\mathbf{D}_{nh}=\frac{1}{N}$.

Obviously $\mathbf{K}_{uC}=0$ and the last term writes:

$$\begin{aligned}\mathbf{K}_{uT}&=-\frac{\partial\int_\Omega\mathbf{B}^T\boldsymbol{\sigma}d\Omega}{\partial\mathbf{u}}-\frac{\partial\int_\Omega\mathbf{N}^T\mathbf{b}d\Omega}{\partial\mathbf{u}}\\ &=\int_\Omega\mathbf{B}^T\frac{\partial\boldsymbol{\sigma}}{\partial T}\frac{\partial T}{\partial\mathbf{u}}\\ &=\int_\Omega\mathbf{B}^T\mathbf{D}_{mt}\mathbf{N}d\Omega+\left(\rho_s-\rho_f\right)\int_\Omega\mathbf{N}^T\mathbf{g}\mathbf{D}_{nt}\mathbf{N}d\Omega\end{aligned}\tag{A7}$$

where $\mathbf{D}_{nt}=-3\alpha_\phi$ and $\mathbf{D}_{mt}=\begin{bmatrix}-3\alpha K & -3\alpha K & -3\alpha K & 0 & 0 & 0\end{bmatrix}^T$.

Jacobian of H equation

Recalling Equation (46), the HM coupling Jacobians can be expanded as

$$\mathbf{K}_{Pu}=-\frac{\partial P}{\partial\mathbf{u}}=-\frac{1}{\Delta t}\frac{\partial\int_\Omega\mathbf{N}^T\rho_f\left[\nabla\cdot\left(\mathbf{u}^{t+\Delta t}\right)-\nabla\cdot\left(\mathbf{u}^t\right)\right]d\Omega}{\partial\mathbf{u}}\tag{A8}$$

Since $\varepsilon_v=\nabla^T\mathbf{u}=\nabla^T\mathbf{N}\mathbf{u}$ with

$$\nabla^T \mathbf{N} = \begin{bmatrix} \frac{\partial}{\partial x} & \frac{\partial}{\partial y} & \frac{\partial}{\partial z} \end{bmatrix} \begin{bmatrix} N_1 & 0 & 0 & N_2 & 0 & 0 & \dots & N_n & 0 & 0 \\ 0 & N_1 & 0 & 0 & N_2 & 0 & \dots & 0 & N_n & 0 \\ 0 & 0 & N_1 & 0 & 0 & N_2 & \dots & 0 & 0 & N_n \end{bmatrix} =$$

$$\begin{bmatrix} \frac{\partial N_1}{\partial x} & \frac{\partial N_1}{\partial y} & \frac{\partial N_1}{\partial z} & \frac{\partial N_2}{\partial x} & \frac{\partial N_2}{\partial y} & \frac{\partial N_2}{\partial z} & \dots & \frac{\partial N_n}{\partial x} & \frac{\partial N_n}{\partial y} & \frac{\partial N_n}{\partial z} \end{bmatrix}$$

Equation (A8) can be rewritten as

$$\mathbf{K}_{Pu} = -\frac{\partial P}{\partial} \quad \int_\Omega \mathbf{N}^T \mathbf{D}_{nm} \mathbf{B} d\Omega + \frac{1}{\Delta t} \int_\Omega \mathbf{N}^T n \rho_f \nabla^T \mathbf{N} d\Omega$$
$$+ \int_\Omega \mathbf{N}^T \rho_f \quad + \int_\Omega \mathbf{N}^T \mathbf{D}_{nm} \mathbf{B} \left(\frac{\rho_f}{K^f} \right) \tag{A9}$$

Regarding the Jacobian of H equation with respect to pressure, we have

$$\mathbf{K}_{PP} = -\frac{\partial \Gamma}{\partial} \quad \frac{\partial \int_\Omega \mathbf{N}^T \quad \mathbf{N}^T n \left(\right.}{\partial} \quad \frac{\partial}{\partial}$$
$$+ \frac{\partial \int_\Omega \mathbf{N}^T n^{t+\Delta t} \quad (\nabla \mathbf{N})^T \quad d\Omega}{\partial} \tag{A10}$$

According to $\frac{\partial \int_\Omega (\nabla \mathbf{N})^T \quad d\Omega}{\partial} = -\int_\Omega (\nabla \mathbf{N})^T \frac{\rho_f k}{\mu_d} (\nabla \mathbf{N}) d\Omega$, Equation (A10) finally gives:

$$\mathbf{K}_{PP} = -\frac{\partial \Gamma}{\partial} \quad \int_\Omega \mathbf{N}^T \mathbf{D}_{nh} \mathbf{B} d\Omega + \frac{1}{\Delta t} \int_\Omega \mathbf{N}^T n \frac{\rho_f}{K^f} \mathbf{N} d\Omega$$
$$+ \int_\Omega \mathbf{N}^T \mathbf{D}_{nh} \mathbf{N} \left(\frac{\rho_f}{K^f} \right)$$
$$+ \int_\Omega \mathbf{N}^T \mathbf{D}_{nh} \mathbf{N} \rho_f \quad \Omega + \frac{\rho_f \kappa}{\mu} \int_\Omega (\nabla \mathbf{N})^T (\nabla \mathbf{N}) d\Omega \tag{A11}$$

Similarly, $\mathbf{K}_{PC} = 0$ and $\mathbf{K}_{PT}$ can be written as:

$$\mathbf{K}_{PT} = -\frac{\partial R}{\partial} \quad \int_\Omega \mathbf{N}^T \mathbf{D}_{nt} \mathbf{N} d\Omega$$
$$+ \frac{\rho_f}{K^f} \int_\Omega \mathbf{N}^T \mathbf{D}_{nT} \mathbf{N}$$
$$- \frac{3 \rho_f \alpha_f}{\Delta t} \int_\Omega \mathbf{N}^T n T \mathbf{N} d\Omega + \int_\Omega \mathbf{N}^T \rho_f \tag{A12}$$

Jacobian of C equation

Considering Equation (47), the first component $\mathbf{K}_{cu}$ can be derived as:

$$\mathbf{K}_{Cu} = -\frac{\partial P}{\partial \quad} \quad \frac{\partial n}{\partial \quad} \quad \frac{\partial n}{\partial \quad} \quad \frac{\partial n}{\partial \quad}$$
$$= \int_\Omega \mathbf{N}^T \mathbf{D}_{nm} \mathbf{B} \quad \frac{}{\Delta t} \int_\Omega \mathbf{N}^T C \mathbf{D}_{nm} \mathbf{B} d\Omega + \int_\Omega \mathbf{N}^T C \mathbf{D}_{nm} \mathbf{B}$$
(A13)

Regarding the Jacobian of C equation with respect to pressure, we have

$$\mathbf{K}_{CP} = \frac{\partial \int_\Omega \mathbf{N}^T n \quad \mathbf{N}^T C \quad \mathbf{N}^T (C n) \nabla \quad d\Omega \quad \partial \int \quad (C \quad) \nabla \mathbf{N} d\Omega}{\partial \quad_f \quad \partial \quad_f \quad \partial \quad_f \quad \rho_f \quad \partial \quad_f}$$
$$= \int_\Omega \mathbf{N}^T \mathbf{D}_{nh} \mathbf{N} \quad \frac{}{\Delta t} \int_\Omega \mathbf{N}^T C \mathbf{D}_{nh} \mathbf{N} d\Omega$$
$$+ \int_\Omega \mathbf{N}^T C \mathbf{D}_{nh} \mathbf{N} \quad \frac{\kappa}{\mu} \int_\Omega C (\nabla \mathbf{N})^T \nabla \mathbf{N} d\Omega$$
(A14)

Considering $\frac{\partial \int_\Omega \mathbf{q}_C \cdot \nabla \mathbf{N} d\Omega}{\partial \quad} \quad -\int_\Omega (\nabla \mathbf{N})^T D_C \nabla \mathbf{N} d\Omega$, $\mathbf{K}_{CC}$ can be written as:

$$\mathbf{K}_{CC} = -\frac{\partial F}{\partial \quad} \quad \frac{1}{\Delta t} \int_\Omega \mathbf{N}^T n \mathbf{N} d\Omega + \int_\Omega \mathbf{N}^T \mathbf{N}$$
$$+ \int_\Omega \mathbf{N}^T n \mathbf{N} \quad \frac{}{\rho_f} \int_\Omega \mathbf{N}^T \mathbf{q}_f \nabla \mathbf{N} d\Omega + \int_\Omega (\nabla \mathbf{N})^T D_C \nabla \mathbf{N} d\Omega$$
(A15)

The last component can be similarly derived as:

$$\mathbf{K}_{CT} = -\frac{\partial F}{\partial \quad} \quad \mathbf{D}_{nt} \mathbf{N} \quad \frac{}{\Delta t} \int_\Omega \mathbf{N}^T C \mathbf{D}_{nt} \mathbf{N} d\Omega + \int_\Omega \mathbf{N}^T C \mathbf{D}_{nt} \mathbf{N}$$
(A16)

Jacobian of T equation

Regarding Equation (48), the TM coupling Jacobians can be expanded as:

$$\mathbf{K}_{Tu} = -\frac{\partial P}{\partial \quad} \quad \frac{\partial n}{\partial \quad}$$
$$+ \frac{1}{\Delta t} \frac{\partial \int_\Omega \mathbf{N}^T \left[(1-n) \rho_s c_s + n \rho_f c \right] T (\nabla \cdot \mathbf{u}^{t+\Delta t} - \nabla \cdot \mathbf{u}^t) d\Omega}{\partial \quad}$$
$$+ c_f \rho_f \left(\frac{}{K^f} - 3\alpha_f \right) \quad \frac{\partial n}{\partial \quad} \quad \frac{\partial n}{\partial \quad} \quad \frac{\partial n}{\partial \quad}$$
$$= -\rho_s c_s \int_\Omega \mathbf{N}^T \mathbf{D}_{nm} \mathbf{B} \quad \frac{}{\Delta t} \int_\Omega \mathbf{N}^T \mathbf{D}_{nm} \mathbf{B}$$
$$+ \frac{1}{\Delta t} \int_\Omega \mathbf{N}^T \left[(1-n) \rho_s c_s + n \rho_f c_f \right] T \nabla^T \mathbf{N} d\Omega + c_f \rho_f \left(\quad \right) \quad \mathbf{B} d\Omega$$
$$- \int_\Omega \mathbf{N}^T \rho_s c_s \mathbf{D}_{nm} \mathbf{B} T$$
(A17)

For the TH coupling term, we have

$$
\begin{aligned}
\mathbf{K}_{TP} &= -\frac{\partial F}{\partial p_f} \int_\Omega \mathbf{N}^T \mathbf{D}_{nh} \mathbf{N} d\Omega \\
&- \frac{1}{\Delta t}\int_\Omega \mathbf{N}^T T c_s \rho_s \frac{1}{N}\mathbf{N} d\Omega + \frac{1}{\Delta t}\int_\Omega \mathbf{N}^T T \left(c_f \rho_f - c_s \rho_s\right) \mathbf{D}_{nh} \mathbf{N} d\Omega \\
&+ \frac{1}{\Delta t}\int_\Omega \mathbf{N}^T T c_f n \frac{\rho_f}{K^f}\mathbf{N} d\Omega + c_f \rho_f \left(i \right. \\
&+ \int_\Omega \mathbf{N}^T \left[-\rho_s c_s + \rho_f c_f\right] \mathbf{D}_{nh} \mathbf{N} T i \qquad \frac{\rho_f \kappa}{\mu}\int_\Omega T \left(\nabla \mathbf{N}\right)^T \nabla \mathbf{N} d\Omega
\end{aligned} \tag{A18}
$$

Obviously $\mathbf{K}_{TC} = 0$ and the last term writes:

$$
\begin{aligned}
\mathbf{K}_{TT} &= -\frac{\partial F}{\partial T} \quad \Delta t \int_\Omega \mathbf{N}^T \left[\left(1-n\right)\rho_s c_s + n\rho_f c_f\right]\mathbf{N} d\Omega - \frac{6 c_s \rho_s \alpha}{\Delta t}\int_\Omega \mathbf{N}^T T \alpha_\phi \mathbf{N} d\Omega \\
&+ \left(c_f \rho_f - c_s \rho_s\right)\left(\frac{1}{\Delta t}\int_\Omega \mathbf{N}^T T \mathbf{D}_{nT} \mathbf{N} d\Omega + \int_\Omega \mathbf{N}^T i \right. \\
&+ \int_\Omega \mathbf{N}^T \mathbf{N} c_f n \rho_f \left(i \right. \\
&- \frac{6\rho_f \alpha_f}{\Delta} \int \mathbf{N}^T T c_f n \mathbf{N} d\Omega + \left[\left(1-n\right)\rho_s c_s + n\rho_f c_f\right]\int_\Omega \mathbf{N}^T \mathbf{N} i \\
&+ \left(\rho_f c_f - \rho_s c_s\right)\int_\Omega \mathbf{N}^T \mathbf{D}_{nT} \mathbf{N} T i \qquad \int_\Omega \mathbf{N}^T \left(\mathbf{q}_f\right)^T \nabla \mathbf{N} d\Omega + \int_\Omega \left(\nabla \mathbf{N}\right)^T \kappa \left(\nabla \mathbf{N}\right) d\Omega
\end{aligned} \tag{A19}
$$

Numerical integration

Targeting at the generalized 3D analysis, a cubic eight-node element (C3D8) with 2×2×2 Gaussian quadrature points is employed for numerical integration in terms of an arbitrary function *f*:

$$
\begin{aligned}
\int_\Omega f\left(x,y,z\right) d\Omega &= \int_{-1}^{1}\int_{-1}^{1}\int_{-1}^{1} \det \mathbf{J} f\left(\xi,\eta,\zeta\right) d\xi d\eta d\zeta \\
&\approx \sum_{i=1}^{2}\sum_{j=1}^{2}\sum_{k=1}^{2} W_i W_j W_k \det \mathbf{J} f\left(\xi,\eta,\zeta\right)
\end{aligned} \tag{A20}
$$

where **J** is also called Jacobian matrix in isoparametric mapping defined by:

$$
\mathbf{J} = \begin{bmatrix}
\frac{\partial x}{\partial \xi} & \frac{\partial y}{\partial \xi} & \frac{\partial z}{\partial \xi} \\
\frac{\partial x}{\partial \eta} & \frac{\partial y}{\partial \eta} & \frac{\partial z}{\partial \eta} \\
\frac{\partial x}{\partial \zeta} & \frac{\partial y}{\partial \zeta} & \frac{\partial z}{\partial \zeta}
\end{bmatrix} \tag{A21}
$$

The final expressions of residuals and Jacobians implemented in the UEL are summarized below. Note the surface flux terms in residuals Equations (45) - (48) are excluded in the final implementation since the natural boundary conditions of the M, H, C and T fields applied on $\partial\Omega_t$

(Equation (31)), $\partial\Omega_H^N$ (Equation (32)), $\partial\Omega_C^N$ and $\partial\Omega_{C,f}^N$ (Equation (33)), $\partial\Omega_T^N$ and $\partial\Omega_{T,f}^N$ (Equation (34)) are handled by Abaqus CAE.

$$\mathbf{R}_{\mathbf{M}} = -\sum_{i=1}^{2}\sum_{j=1}^{2}\sum_{k=1}^{2} W_i W_j W_k \det\mathbf{J}\mathbf{B}^T\left(\xi_i,\eta_j,\zeta_k\right)\boldsymbol{\sigma}\left(\xi_i,\eta_j,\zeta_k\right) + \sum_{i=1}^{2}\sum_{j=1}^{2}\sum_{k=1}^{2} W_i W_j W_k \det\mathbf{J}\mathbf{N}^T\left(\xi_i,\eta_j,\zeta_k\right)\left[n\rho_f + \left(1-n\right)\rho_s\right]\mathbf{g} \tag{A22}$$

$$R_H = -\sum_{i=1}^{2}\sum_{j=1}^{2}\sum_{k=1}^{2} W_i W_j W_k \det\mathbf{J}\mathbf{N}^T\left(\xi_i,\eta_j,\zeta_k\right)\rho_f i - \sum_{i=1}^{2}\sum_{j=1}^{2}\sum_{k=1}^{2} W_i W_j W_k \det\mathbf{J}\mathbf{N}^T\left(\xi_i,\eta_j,\zeta_k\right)n\left(\frac{\rho_f}{K^f} i \right. \tag{A23}$$

$$-\frac{1}{\Delta t}\sum_{i=1}^{2}\sum_{j=1}^{2}\sum_{k=1}^{2} W_i W_j W_k \det\mathbf{J}\mathbf{N}^T\left(\xi_i,\eta_j,\zeta_k\right)n\rho_f i \quad \sum_{i=1}^{2}\sum_{j=1}^{2}\sum_{k=1}^{2} W_i W_j W_k \det\mathbf{J}\left(\nabla\mathbf{N}\left(\xi_i,\eta_j,\zeta_k\right)\right)^T\mathbf{q}_f$$

$$R_C = -\sum_{i=1}^{2}\sum_{j=1}^{2}\sum_{k=1}^{2} W_i W_j W_k \det\mathbf{J}\mathbf{N}^T\left(\xi_i,\eta_j,\zeta_k\right)n C - \sum_{i=1}^{2}\sum_{j=1}^{2}\sum_{k=1}^{2} W_i W_j W_k \det\mathbf{J}\mathbf{N}^T\left(\xi_i,\eta_j,\zeta_k\right)C i - \sum_{i=1}^{2}\sum_{j=1}^{2}\sum_{k=1}^{2} W_i W_j W_k \det\mathbf{J}\mathbf{N}^T\left(\xi_i,\eta_j,\zeta_k\right)(Cn) i + \sum_{i=1}^{2}\sum_{j=1}^{2}\sum_{k=1}^{2} W_i W_j W_k \det\mathbf{J}\frac{C}{\rho_f}\left(\mathbf{q}_f\right)^T\nabla\mathbf{N}\left(\xi_i,\eta_j,\zeta_k\right) + \sum_{i=1}^{2}\sum_{j=1}^{2}\sum_{k=1}^{2} W_i W_j W_k \det\mathbf{J}\left(\mathbf{q}_C\right)^T\nabla\mathbf{N}\left(\xi_i,\eta_j,\zeta_k\right) \tag{A24}$$

$$R_T = -\sum_{i=1}^{2}\sum_{j=1}^{2}\sum_{k=1}^{2} W_i W_j W_k \det\mathbf{J}\mathbf{N}^T\left(\xi_i,\eta_j,\zeta_k\right)\left[\left(1-n\right)\rho_s c_s + n\rho_f c_f\right] i + \sum_{i=1}^{2}\sum_{j=1}^{2}\sum_{k=1}^{2} W_i W_j W_k \det\mathbf{J}\mathbf{N}^T\left(\xi_i,\eta_j,\zeta_k\right)T c_s\rho_s\left(\left(1-b\right) i \right.$$

$$-\sum_{i=1}^{2}\sum_{j=1}^{2}\sum_{k=1}^{2} W_i W_j W_k \det\mathbf{J}\mathbf{N}^T\left(\xi_i,\eta_j,\zeta_k\right)T\left(c_f\rho_f - c_s\rho_s\right) i - \sum_{i=1}^{2}\sum_{j=1}^{2}\sum_{k=1}^{2} W_i W_j W_k \det\mathbf{J}\mathbf{N}^T\left(\xi_i,\eta_j,\zeta_k\right)T c_f n\rho_f\left(i \quad \alpha_f i \right. \tag{A25}$$

$$-\sum_{i=1}^{2}\sum_{j=1}^{2}\sum_{k=1}^{2} W_i W_j W_k \det\mathbf{J}\mathbf{N}^T\left(\xi_i,\eta_j,\zeta_k\right)\left[\left(1-n\right)\rho_s c_s + n\rho_f c_f\right] T i + \sum_{i=1}^{2}\sum_{j=1}^{2}\sum_{k=1}^{2} W_i W_j W_k \det\mathbf{J}\left(\nabla\mathbf{N}\right)^T\left(\xi_i,\eta_j,\zeta_k\right)c_f T\mathbf{q}_f + \sum_{i=1}^{2}\sum_{j=1}^{2}\sum_{k=1}^{2} W_i W_j W_k \det\mathbf{J}\left(\nabla\mathbf{N}\right)\left(\xi_i,\eta_j,\zeta_k\right)^T\mathbf{q}_T$$

$$\mathbf{K}_{uu}=\sum_{i=1}^{2}\sum_{j=1}^{2}\sum_{k=1}^{2}W_iW_jW_k\det\mathbf{JB}^T\left(\xi_i,\eta_j,\zeta_k\right)\mathbf{D}_{mm}\mathbf{B}\left(\xi_i,\eta_j,\zeta_k\right)$$
$$+\left(\rho_s-\rho_f\right)\sum_{i=1}^{2}\sum_{j=1}^{2}\sum_{k=1}^{2}W_iW_jW_k\det\mathbf{JN}^T\left(\xi_i,\eta_j,\zeta_k\right)\mathbf{g}\mathbf{D}_{nm}\mathbf{B}\left(\xi_i,\eta_j,\zeta_k\right) \quad \text{(A26)}$$

$$\mathbf{K}_{uP}=\sum_{i=1}^{2}\sum_{j=1}^{2}\sum_{k=1}^{2}W_iW_jW_k\det\mathbf{JB}^T\left(\xi_i,\eta_j,\zeta_k\right)\mathbf{D}_{mh}\mathbf{N}\left(\xi_i,\eta_j,\zeta_k\right)$$
$$+\left(\rho_s-\rho_f\right)\sum_{i=1}^{2}\sum_{j=1}^{2}\sum_{k=1}^{2}W_iW_jW_k\det\mathbf{JN}^T\left(\xi_i,\eta_j,\zeta_k\right)\mathbf{g}\mathbf{D}_{nh}\mathbf{N}\left(\xi_i,\eta_j,\zeta_k\right) \quad \text{(A27)}$$

$$\mathbf{K}_{uT}=\sum_{i=1}^{2}\sum_{j=1}^{2}\sum_{k=1}^{2}W_iW_jW_k\det\mathbf{JB}^T\left(\xi_i,\eta_j,\zeta_k\right)\mathbf{D}_{mt}\mathbf{N}\left(\xi_i,\eta_j,\zeta_k\right)$$
$$+\left(\rho_s-\rho_f\right)\sum_{i=1}^{2}\sum_{j=1}^{2}\sum_{k=1}^{2}W_iW_jW_k\det\mathbf{JN}^T\left(\xi_i,\eta_j,\zeta_k\right)\mathbf{g}\mathbf{D}_{nt}\mathbf{N}\left(\xi_i,\eta_j,\zeta_k\right) \quad \text{(A28)}$$

$$\mathbf{K}_{Pu}=\frac{1}{\Delta t}\rho_f\sum_{i=1}^{2}\sum_{j=1}^{2}\sum_{k=1}^{2}W_iW_jW_k\det\mathbf{JN}^T\left(\xi_i,\eta_j,\zeta_k\right)\mathbf{D}_{nm}\mathbf{B}\left(\xi_i,\eta_j,\zeta_k\right)$$
$$+\frac{1}{\Delta t}\rho_f\sum_{i=1}^{2}\sum_{j=1}^{2}\sum_{k=1}^{2}W_iW_jW_k\det\mathbf{JN}^T\left(\xi_i,\eta_j,\zeta_k\right)\nabla\mathbf{N}^T\left(\xi_i,\eta_j,\zeta_k\right)$$
$$+\rho_f\sum_{i=1}^{2}\sum_{j=1}^{2}\sum_{k=1}^{2}W_iW_jW_k\det\mathbf{JN}^T\left(\xi_i,\eta_j,\zeta_k\right)\dot{\quad}\qquad\qquad,\eta_j,\zeta_k\right) \quad \text{(A29)}$$
$$+\sum_{i=1}^{2}\sum_{j=1}^{2}\sum_{k=1}^{2}W_iW_jW_k\det\mathbf{JN}^T\left(\xi_i,\eta_j,\zeta_k\right)\mathbf{D}_{nm}\mathbf{B}\left(\xi_i,\eta_j,\zeta_k\right)\left(\rho_f\dot{\quad}\right.$$

$$\mathbf{K}_{PP}=\frac{\rho_f}{\Delta t}\sum_{i=1}^{2}\sum_{j=1}^{2}\sum_{k=1}^{2}W_iW_jW_k\det\mathbf{JN}^T\left(\xi_i,\eta_j,\zeta_k\right)\mathbf{D}_{nh}\mathbf{N}\left(\xi_i,\eta_j,\zeta_k\right)$$
$$+\frac{1}{\Delta t}\frac{\rho_f}{K^f}\sum_{i=1}^{2}\sum_{j=1}^{2}\sum_{k=1}^{2}W_iW_jW_k\det\mathbf{JN}^T\left(\xi_i,\eta_j,\zeta_k\right)n\mathbf{N}\left(\xi_i,\eta_j,\zeta_k\right)$$
$$+\sum_{i=1}^{2}\sum_{j=1}^{2}\sum_{k=1}^{2}W_iW_jW_k\det\mathbf{JN}^T\left(\xi_i,\eta_j,\zeta_k\right)\mathbf{D}_{nh}\mathbf{N}\left(\xi_i,\eta_j,\zeta_k\right)\left(\rho_f\dot{\quad}\right. \quad \text{(A30)}$$
$$+\sum_{i=1}^{2}\sum_{j=1}^{2}\sum_{k=1}^{2}W_iW_jW_k\det\mathbf{JN}^T\left(\xi_i,\eta_j,\zeta_k\right)\mathbf{D}_{nh}\mathbf{N}\rho_f\dot{}$$
$$+\frac{\rho_f\kappa}{\mu}\sum_{i=1}^{2}\sum_{j=1}^{2}\sum_{k=1}^{2}W_iW_jW_k\det\mathbf{J}\left(\nabla\cdot\mathbf{N}\left(\xi_i,\eta_j,\zeta_k\right)\right)^T\left(\nabla\cdot\mathbf{N}\left(\xi_i,\eta_j,\zeta_k\right)\right)$$

$$\mathbf{K}_{PT}=\frac{\rho_f}{\Delta t}\sum_{i=1}^{2}\sum_{j=1}^{2}\sum_{k=1}^{2}W_iW_jW_k\det\mathbf{JN}^T\left(\xi_i,\eta_j,\zeta_k\right)\mathbf{D}_{nt}\mathbf{N}\left(\xi_i,\eta_j,\zeta_k\right)$$
$$+\frac{\rho_f}{K^f}\sum_{i=1}^{2}\sum_{j=1}^{2}\sum_{k=1}^{2}W_iW_jW_k\det\mathbf{JN}^T\left(\xi_i,\eta_j,\zeta_k\right)\mathbf{D}_{nt}\mathbf{N}\left(\xi_i,\eta_j,\zeta_k\right)i$$
$$-3\rho_f\alpha_f\sum_{i=1}^{2}\sum_{j=1}^{2}\sum_{k=1}^{2}W_iW_jW_k\det\mathbf{JN}^T\left(\xi_i,\eta_j,\zeta_k\right)\mathbf{D}_{nt}\mathbf{N}\left(\xi_i,\eta_j,\zeta_k\right)i \quad \text{(A31)}$$
$$-\frac{3\rho_f\alpha_f}{\Delta t}\sum_{i=1}^{2}\sum_{j=1}^{2}\sum_{k=1}^{2}W_iW_jW_k\det\mathbf{JN}^T\left(\xi_i,\eta_j,\zeta_k\right)n\mathbf{D}_{nt}\mathbf{N}\left(\xi_i,\eta_j,\zeta_k\right)T$$
$$+\rho_f\sum_{i=1}^{2}\sum_{j=1}^{2}\sum_{k=1}^{2}W_iW_jW_k\det\mathbf{JN}^T\left(\xi_i,\eta_j,\zeta_k\right)\mathbf{D}_{nt}\mathbf{N}\left(\xi_i,\eta_j,\zeta_k\right)i$$

$$\mathbf{K}_{Cu}=\sum_{i=1}^{2}\sum_{j=1}^{2}\sum_{k=1}^{2}W_iW_jW_k\det\mathbf{JN}^T\left(\xi_i,\eta_j,\zeta_k\right)\mathbf{D}_{nm}\mathbf{B}\left(\xi_i,\eta_j,\zeta_k\right)C$$
$$+\frac{1}{\Delta t}\sum_{i=1}^{2}\sum_{j=1}^{2}\sum_{k=1}^{2}W_iW_jW_k\det\mathbf{JN}^T\left(\xi_i,\eta_j,\zeta_k\right)C\mathbf{D}_{nm}\mathbf{B}\left(\xi_i,\eta_j,\zeta_k\right) \quad \text{(A32)}$$
$$+\sum_{i=1}^{2}\sum_{j=1}^{2}\sum_{k=1}^{2}W_iW_jW_k\det\mathbf{JN}^T\left(\xi_i,\eta_j,\zeta_k\right)C\mathbf{D}_{nm}\mathbf{B}\left(\xi_i,\eta_j,\zeta_k\right)i$$

$$\mathbf{K}_{CP}=\sum_{i=1}^{2}\sum_{j=1}^{2}\sum_{k=1}^{2}W_iW_jW_k\det\mathbf{JN}^T\left(\xi_i,\eta_j,\zeta_k\right)\mathbf{D}_{nh}\mathbf{N}\left(\xi_i,\eta_j,\zeta_k\right)C$$
$$+\frac{1}{\Delta t}\sum_{i=1}^{2}\sum_{j=1}^{2}\sum_{k=1}^{2}W_iW_jW_k\det\mathbf{JN}^T\left(\xi_i,\eta_j,\zeta_k\right)C\mathbf{D}_{nh}\mathbf{N}\left(\xi_i,\eta_j,\zeta_k\right)$$
$$+\sum_{i=1}^{2}\sum_{j=1}^{2}\sum_{k=1}^{2}W_iW_jW_k\det\mathbf{JN}^T\left(\xi_i,\eta_j,\zeta_k\right)C\mathbf{D}_{nh}\mathbf{N}\left(\xi_i,\eta_j,\zeta_k\right)i \quad \text{(A33)}$$
$$+\frac{c_f\kappa}{\mu}\sum_{i=1}^{2}\sum_{j=1}^{2}\sum_{k=1}^{2}W_iW_jW_k\det\mathbf{J}C\left(\nabla\mathbf{N}\right)^T\nabla\mathbf{N}\left(\xi_i,\eta_j,\zeta_k\right)$$

$$\mathbf{K}_{CC}=\frac{1}{\Delta t}\sum_{i=1}^{2}\sum_{j=1}^{2}\sum_{k=1}^{2}W_iW_jW_k\det\mathbf{JN}^T\left(\xi_i,\eta_j,\zeta_k\right)n\mathbf{N}\left(\xi_i,\eta_j,\zeta_k\right)$$
$$+\sum_{i=1}^{2}\sum_{j=1}^{2}\sum_{k=1}^{2}W_iW_jW_k\det\mathbf{JN}^T\left(\xi_i,\eta_j,\zeta_k\right)\mathbf{N}\left(\xi_i,\eta_j,\zeta_k\right)i$$
$$+\sum_{i=1}^{2}\sum_{j=1}^{2}\sum_{k=1}^{2}W_iW_jW_k\det\mathbf{JN}^T\left(\xi_i,\eta_j,\zeta_k\right)n\mathbf{N}\left(\xi_i,\eta_j,\zeta_k\right)i \quad \text{(A34)}$$
$$-\frac{1}{\rho_f}\sum_{i=1}^{2}\sum_{j=1}^{2}\sum_{k=1}^{2}W_iW_jW_k\det\mathbf{JN}^T\left(\mathbf{q}_f\right)^T\nabla\mathbf{N}\left(\xi_i,\eta_j,\zeta_k\right)$$
$$+\sum_{i=1}^{2}\sum_{j=1}^{2}\sum_{k=1}^{2}W_iW_jW_k\det\mathbf{J}\left(\nabla\mathbf{N}\left(\xi_i,\eta_j,\zeta_k\right)\right)^T D_C\left(\nabla\mathbf{N}\left(\xi_i,\eta_j,\zeta_k\right)\right)$$

$$\mathbf{K}_{CT}=\sum_{i=1}^{2}\sum_{j=1}^{2}\sum_{k=1}^{2}W_iW_jW_k\det\mathbf{J}\mathbf{N}^T\left(\xi_i,\eta_j,\zeta_k\right)\mathbf{D}_{nt}\mathbf{N}\left(\xi_i,\eta_j,\zeta_k\right)\dot{C}$$
$$+\frac{1}{\Delta t}\sum_{i=1}^{2}\sum_{j=1}^{2}\sum_{k=1}^{2}W_iW_jW_k\det\mathbf{J}\mathbf{N}^T\left(\xi_i,\eta_j,\zeta_k\right)C\mathbf{D}_{nt}\mathbf{N}\left(\xi_i,\eta_j,\zeta_k\right) \quad \text{(A35)}$$
$$+\sum_{i=1}^{2}\sum_{j=1}^{2}\sum_{k=1}^{2}W_iW_jW_k\det\mathbf{J}\mathbf{N}^T\left(\xi_i,\eta_j,\zeta_k\right)C\mathbf{D}_{nt}\mathbf{N}\left(\xi_i,\eta_j,\zeta_k\right)\dot{\varepsilon}$$

$$\mathbf{K}_{Tu}=\sum_{i=1}^{2}\sum_{j=1}^{2}\sum_{k=1}^{2}W_iW_jW_k\det\mathbf{J}\left(\rho_fc_f-\rho_sc_s\right)\mathbf{N}^T\left(\xi_i,\eta_j,\zeta_k\right)\mathbf{D}_{nm}\mathbf{B}\left(\xi_i,\eta_j,\zeta_k\right)\dot{T}$$
$$+\sum_{i=1}^{2}\sum_{j=1}^{2}\sum_{k=1}^{2}W_iW_jW_k\det\mathbf{J}c_f\rho_f\left(\dot{T}\right)T\mathbf{D}_{nm}\mathbf{B}\left(\xi_i,\eta_j,\zeta_k\right)$$
$$+\frac{1}{\Delta t}\sum_{i=1}^{2}\sum_{j=1}^{2}\sum_{k=1}^{2}W_iW_jW_k\det\mathbf{J}\mathbf{N}^T\left(\xi_i,\eta_j,\zeta_k\right)\left[\left(1-n\right)\rho_sc_s+n\rho_fc_f\right]T\nabla^T\mathbf{N}\left(\xi_i,\eta_j,\zeta_k\right) \quad \text{(A36)}$$
$$-\sum_{i=1}^{2}\sum_{j=1}^{2}\sum_{k=1}^{2}W_iW_jW_k\det\mathbf{J}\mathbf{N}^T\left(\xi_i,\eta_j,\zeta_k\right)\rho_sc_s\mathbf{D}_{nm}\mathbf{B}\left(\xi_i,\eta_j,\zeta_k\right)T\dot{\varepsilon}$$
$$+\sum_{i=1}^{2}\sum_{j=1}^{2}\sum_{k=1}^{2}W_iW_jW_k\det\mathbf{J}\mathbf{N}^T\left(\xi_i,\eta_j,\zeta_k\right)\rho_fc_f\mathbf{D}_{nm}\mathbf{B}\left(\xi_i,\eta_j,\zeta_k\right)T\dot{\varepsilon}$$

$$\mathbf{K}_{TP}=\sum_{i=1}^{2}\sum_{j=1}^{2}\sum_{k=1}^{2}W_iW_jW_k\det\mathbf{J}\left(\rho_fc_f-\rho_sc_s\right)\mathbf{N}^T\left(\xi_i,\eta_j,\zeta_k\right)\mathbf{D}_{nh}\mathbf{N}\left(\xi_i,\eta_j,\zeta_k\right)\dot{T}$$
$$-\frac{1}{\Delta t}\sum_{i=1}^{2}\sum_{j=1}^{2}\sum_{k=1}^{2}W_iW_jW_k\det\mathbf{J}\mathbf{N}^T\left(\xi_i,\eta_j,\zeta_k\right)Tc_s\rho_s\frac{1}{N}\mathbf{N}\left(\xi_i,\eta_j,\zeta_k\right)$$
$$+\frac{1}{\Delta t}\sum_{i=1}^{2}\sum_{j=1}^{2}\sum_{k=1}^{2}W_iW_jW_k\det\mathbf{J}\mathbf{N}^T\left(\xi_i,\eta_j,\zeta_k\right)T\left(c_f\rho_f-c_s\rho_s\right)\mathbf{D}_{nh}\mathbf{N}\left(\xi_i,\eta_j,\zeta_k\right)$$
$$+\frac{1}{\Delta t}\sum_{i=1}^{2}\sum_{j=1}^{2}\sum_{k=1}^{2}W_iW_jW_k\det\mathbf{J}\mathbf{N}^T\left(\xi_i,\eta_j,\zeta_k\right)Tc_fn\frac{\rho_f}{K^f}\mathbf{N}\left(\xi_i,\eta_j,\zeta_k\right) \quad \text{(A37)}$$
$$+\sum_{i=1}^{2}\sum_{j=1}^{2}\sum_{k=1}^{2}W_iW_jW_k\det\mathbf{J}\rho_fc_f\left(\dot{T}\right)$$
$$+\sum_{i=1}^{2}\sum_{j=1}^{2}\sum_{k=1}^{2}W_iW_jW_k\det\mathbf{J}\mathbf{N}^T\left(\xi_i,\eta_j,\zeta_k\right)\left(-\rho_sc_s+\rho_fc_f\right)\mathbf{D}_{nh}\mathbf{N}\left(\xi_i,\eta_j,\zeta_k\right)T\dot{\varepsilon}$$
$$+\sum_{i=1}^{2}\sum_{j=1}^{2}\sum_{k=1}^{2}W_iW_jW_k\det\mathbf{J}T\left(\nabla\mathbf{N}\right)^T\nabla\mathbf{N}\left(\xi_i,\eta_j,\zeta_k\right)c_f\rho_f\kappa/\mu$$

$$\begin{aligned}
\mathbf{K}_{TT} &= \frac{1}{\Delta t}\sum_{i=1}^{2}\sum_{j=1}^{2}\sum_{k=1}^{2} W_i W_j W_k \det \mathbf{J}\mathbf{N}^T\left(\xi_i,\eta_j,\zeta_k\right)\left[\left(1-n\right)\rho_s c_s + n\rho_f c_f\right]\mathbf{N}\left(\xi_i,\eta_j,\zeta_k\right)\\
&-\frac{6c_s\rho_s\alpha}{\Delta t}\sum_{i=1}^{2}\sum_{j=1}^{2}\sum_{k=1}^{2} W_i W_j W_k \det \mathbf{J}\mathbf{N}^T\left(\xi_i,\eta_j,\zeta_k\right)T\alpha_\phi\mathbf{N}\left(\xi_i,\eta_j,\zeta_k\right)\\
&+\sum_{i=1}^{2}\sum_{j=1}^{2}\sum_{k=1}^{2} W_i W_j W_k \det \mathbf{J}\mathbf{N}^T\left(\xi_i,\eta_j,\zeta_k\right)\left(c_f\rho_f - c_s\rho_s\right)\left(\text{¿}\ \text{[illegible]}\ \frac{\text{[illegible]}}{\Delta t}\right)\mathbf{N}\left(\xi_i,\eta_j,\zeta_k\right)\\
&+\sum_{i=1}^{2}\sum_{j=1}^{2}\sum_{k=1}^{2} W_i W_j W_k \det \mathbf{J}\mathbf{N}^T\left(\xi_i,\eta_j,\zeta_k\right)\rho_f\left(\text{[illegible]}\right._{f}\mathbf{N}\left(\xi_i,\eta_j,\zeta_k\right)\\
&-\frac{6\rho_f\alpha_f}{\triangle}\sum^{2}\sum^{2}_{\text{[illegible]}1}\sum_{k=1}^{2} W_i W_j W_k \det \mathbf{J}\mathbf{N}^T\left(\xi_i,\eta_j,\zeta_k\right)Tc_f n\mathbf{N}\left(\xi_i,\eta_j,\zeta_k\right)\\
&+\sum_{i=1}^{2}\sum_{j=1}^{2}\sum_{k=1}^{2} W_i W_j W_k \det \mathbf{J}\mathbf{N}^T\left(\xi_i,\eta_j,\zeta_k\right)\left[\left(1-n\right)\rho_s c_s + n\rho_f c_f\right]\mathbf{N}\left(\xi_i,\eta_j,\zeta_k\right)\text{¿}\\
&+\sum_{i=1}^{2}\sum_{j=1}^{2}\sum_{k=1}^{2} W_i W_j W_k \det \mathbf{J}\mathbf{N}^T\left(\xi_i,\eta_j,\zeta_k\right)\left(-\rho_s c_s + \rho_f c_f\right)\mathbf{D}_{nT}\mathbf{N}\left(\xi_i,\eta_j,\zeta_k\right)T\text{¿}\\
&-\sum_{i=1}^{2}\sum_{j=1}^{2}\sum_{k=1}^{2} W_i W_j W_k \det \mathbf{J}\mathbf{N}^T\left(\xi_i,\eta_j,\zeta_k\right)c_f\left(\mathbf{q}_f\right)^T\nabla\mathbf{N}\left(\xi_i,\eta_j,\zeta_k\right)\\
&+\sum_{i=1}^{2}\sum_{j=1}^{2}\sum_{k=1}^{2} W_i W_j W_k \det \mathbf{J}T\left(\nabla\mathbf{N}\left(\xi_i,\eta_j,\zeta_k\right)\right)^T\nabla\mathbf{N}\left(\xi_i,\eta_j,\zeta_k\right)\kappa
\end{aligned}\tag{A38}$$

Table 1 Governing equations* for the coupled THMC processes

Physics	unknowns	Governing equations
M (mechanical)	**u**	$\nabla\cdot\boldsymbol{\sigma}+\mathbf{b}=0$ with $\mathbf{b}=\left[n\rho_f+(1-n)\rho_s\right]\mathbf{g}$
H (hydraulic)	P_f	ρ_f [illegible] $=0$
C (Chemical)	C	$n($ [illegible] $-\mathbf{q}_f\Big)+\nabla\cdot\mathbf{q}_C=0$
T (Thermal)	T	$\left[(1-n)\rho_s c_s+n\rho_f c_f\right]$ [illegible] $T\begin{cases}-c_s\rho_s\left[(1-b)\right.$ [illegible] $+\left(c_f\rho_f-c_s\rho_s\right)$ [illegible] $+\left[(1-n)\rho_s c_s T+n\rho_f c_f T\right]$ [illegible] $T\mathbf{q}_f\Big)+\nabla\cdot\mathbf{q}_T=0$

* Note that **σ**, n, ε_v, $\mathbf{q}_f$, $\mathbf{q}_c$, $\mathbf{q}_t$ are intermediate variables. They can be expressed in terms of the unknowns [**u**, P_f, C, T] via constitutive relation Equation (23), strain-displacement relation Equation(19), and conduction laws Equation (28).

Table 2: Material properties for FE simulation

Parameter	Symbol	Value	Unit
Shear modulus	G	300	MPa
Bulk modulus	K	300	MPa
Solid density	ρ_s	2670	kg/m^3
Fluid density	P_f	1000	kg/m^3
Fluid tangent bulk modulus	K_f	3000	MPa
Initial porosity	n_0	0.4	
Permeability	k	2.6×10^{-19}	m^2
Dynamic viscosity	μ	0.001	Pa·s
Biot tangent modulus	N	3.0×10^{5}	MPa
Biot coefficient	b	0.9	
Diffusivity	D_c	8.0×10^{-10}	m^2/s
Thermal conductivity	κ	1.4	W/(m·K)
Solid specific heat	c_s	835	J/(kg·K)
Fluid specific heat	c_f	4202	J/(kg·K)
Solid thermal expansion coefficient	α	5.0×10^{-5}	K^{-1}
Thermal expansion coefficient related to porosity	α_ϕ	4.0×10^{-5}	K^{-1}
Fluid thermal expansion coefficient	α_f	1.0×10^{-4}	K^{-1}